

1 **O₃ and PAN in southern Tibetan Plateau determined by distinct** 2 **physical and chemical processes**

3 Wanyun Xu¹, Yuxuan Bian¹, Weili Lin², Yingjie Zhang^{3,a}, Yaru Wang^{3,b}, Xiaoyi Zhang^{1,4}, Gen Zhang^{1,*},
4 Chunxiang Ye^{3,*}, Xiaobin Xu¹

5 ¹ State Key Laboratory of Severe Weather & Key Laboratory for Atmospheric Chemistry of CMA, Institute of Atmospheric
6 Composition, Chinese Academy of Meteorological Sciences, Beijing, 100081, China

7 ² College of Life and Environmental Sciences, Minzu University of China, Beijing, 100081, China

8 ³ College of Environment, Peking University of China, Beijing, 100871, China

9 ⁴ Department of Atmospheric and Oceanic Sciences, Fudan University, Shanghai, 200433, China

10 ^a now at School of Ecology and Nature Conservation, Beijing Forestry University, Beijing, 100083, China

11 ^b now at Leibniz Institute for Tropospheric Research, Leipzig, 04318, Germany

12 *Correspondence to:* Gen Zhang (zhanggen@cma.gov.cn) and Chunxiang Ye (c.ye@pku.edu.cn)

13 **Abstract.** Tropospheric ozone (O₃) and peroxyacetyl nitrate (PAN) are both photochemical pollutants harmful to the
14 ecological environment and human health. In this study, measurements of O₃ and PAN as well as their precursors were
15 conducted from May to July 2019 at Nam Co station (NMC), a highly pristine high-altitude site in the southern Tibetan
16 Plateau (TP), to investigate how distinct transport processes and photochemistry contributed to their variations. Results
17 revealed that, despite highly similar diurnal variations with steep morning rises and flat daytime plateaus that were caused by
18 boundary layer development and downmixing of free tropospheric air, day to day variations in O₃ and PAN were in fact
19 controlled by distinct physicochemical processes. During the dry spring season, air masses rich in O₃ were associated with
20 high altitude westerly air masses that entered the TP from the west or the south, which frequently carried high loadings of
21 stratospheric O₃ to NMC. During the summer monsoon season, a northward shift of the subtropical jet stream shifted the
22 stratospheric downward entrainment pathway also to the north, leading to direct stratospheric O₃ entrainment into the
23 troposphere of the northern TP, which travelled southwards to NMC within low altitudes via northerly winds in front of
24 ridges or closed high pressures over the TP. Westerly and southerly air masses, however, revealed low O₃ levels due to the
25 overall less stratospheric O₃ within the troposphere of low latitude regions. PAN, however, was only rich in westerly or
26 southerly air masses that crossed over polluted regions such as Northern India, Nepal or Bangladesh before entering the TP
27 and arriving at NMC from the south during both spring and summer. Overall, the O₃ level at NMC was mostly determined
28 by stratosphere-troposphere exchange (STE), which explained 77% and 88% of the observed O₃ concentration in spring and
29 summer, respectively. However, only 0.1% of the springtime day-to-day O₃ variability could be explained by STE processes,
30 while 22% was explained during summertime. Positive net photochemical formation was estimated for both O₃ and PAN
31 based on observation-constrained box modelling. Near surface photochemical formation was unable to account for the high
32 O₃ level observed at NMC, and nor was it the determining factor for the day-to-day variability of O₃. However, it was able to
33 capture events with elevated PAN concentrations and explain its day-to-day variations. O₃ and PAN formation were both
34 highly sensitive to NO_x levels, with PAN being also quite sensitive to VOCs concentrations. The rapid development of

35 transportation networks and urbanization within the TP may lead to increased emissions and loadings in NO_x and VOCs ,
36 resulting in strongly enhanced O_3 and PAN formation in downwind pristine regions, which should be given greater attention
37 in future studies.
38

39 **1 Introduction**

40 Ozone (O_3) and peroxyacetyl nitrate (PAN) are key photochemical pollutants in the troposphere, that are harmful to
41 vegetation and human health (Kleindienst et al., 1990;Yukihiro et al., 2012;Taylor, 1969;Lefohn et al., 2017). Since O_3 and
42 PAN are both produced during the oxidation of volatile organic compounds (VOCs) in the presence of nitrogen oxides (NO_x),
43 they often share highly similar variational characteristics (Fischer et al., 2014). However, PAN is formed only from a limited
44 number of oxygenated VOCs (OVOCs), which are typically oxidation products of alkenes (with low carbon numbers),
45 aromatics and isoprene (Xu et al., 2021), while O_3 can be practically formed from all VOCs. Additionally, the photochemical
46 formation of O_3 depends highly nonlinearly on its precursor concentrations, being insensitive to VOCs changes under NO_x -
47 limited conditions and vice versa, while PAN varied nearly proportionally to its OVOC precursors, with additional
48 influences from the NO_2 to NO ratio (Xu et al., 2021). Thus, photochemistry can sometimes result in distinct variations of O_3
49 and PAN, especially during cold seasons (Xu et al., 2021;Zhang et al., 2020). From the aspect of physical transport, O_3 and
50 PAN can both be transported over large distances. Since PAN is easily thermal decomposed under high temperatures, its
51 transport is more favored in cold seasons or at higher altitudes. Early simulation studies suggested PAN to be an important
52 reservoir for NO_x in the troposphere and lower stratosphere (Singh and Hanst, 1981), redistributing NO_x far from its source
53 regions (Moxim et al., 1996). Different from PAN, O_3 is naturally produced within the stratosphere and can be transported
54 into the troposphere via stratosphere-troposphere exchange (STE) processes that are often associated with the occurrence of
55 tropopause folds, cut-off lows, streamers near the polar-front jet or subtropical jet stream, and mid-latitude cyclones
56 (Langford, 1999;Stohl et al., 2003;Sprenger et al., 2007;Tang et al., 2011). STE elevates tropospheric O_3 and oxidation
57 capacity at distinct latitudes during different seasons, with the largest mass fluxes in summer occurring mostly in higher mid-
58 latitudes, followed by spring occurring mostly in lower mid-latitudes (Tang et al., 2011;Škerlak et al., 2014). Deep STE
59 intrusions reaching the planetary boundary layer (PBL) and associated mass fluxes are largest during spring in China and the
60 western part of North America.

61 While the variational characteristics, influence of photochemical formation and transport on O_3 and PAN have been widely
62 investigated in polluted urban regions of China (Liu et al., 2018;Yao et al., 2019;Hu et al., 2020;Wei et al., 2020;Qiu et al.,
63 2021;Zhang et al., 2021;Xu et al., 2021), those at remote background sites received less attention, especially for PAN. The
64 Tibetan Plateau (TP), located in western China, is often called the “Third Pole” with its average altitude over 4000 m. Due to
65 its harsh environment, the TP is only scarcely populated and thus highly pristine. The topography of the TP affects large
66 scale circulations with its strong thermal forcing, thereby influencing the weather, climate and air quality in eastern China

67 (Yang et al., 2014). Surface O₃ as a crucial greenhouse gas and with its deterministic role on atmospheric oxidation capacity
68 has been paid certain attention in the TP and special attention has been given to the photochemical formation of O₃ under the
69 strong radiative conditions at such high altitudes. Ma et al. (2002) investigated the photochemical formation of O₃ at Mt.
70 Waliguan (WLG) in the Northeastern TP through box-modelling and suggested wintertime net production and summertime
71 net loss in O₃. Xue et al. (2013) further constrained the box model with VOCs sampling results, mainly including
72 hydrocarbons and aromatic compounds (no oxygenated compounds), and found net O₃ formation at WLG during both spring
73 and summer 2003. Airmass transport from central and eastern China was found to be frequent during summertime (Xue et al.,
74 2011; Xu et al., 2018a), revealing higher O₃ production efficiencies (Xue et al., 2011) and being held responsible for rising
75 O₃ trends during summer and autumn (Xu et al., 2016; Xu et al., 2018a). Due to its high altitude, the TP revealed the largest
76 deep STE O₃ mass fluxes, with higher fluxes in spring and winter and lower ones in summer and autumn, especially in the
77 southeastern TP (Škerlak et al., 2014). At WLG, O₃ was observed to be strongly influenced by STE associated with the
78 subtropical jet during spring and summer in 2003, with stronger impacts during summer than spring (Ding and Wang,
79 2006; Zheng et al., 2008). STE was estimated to contribute an annual average of 10.2% to tropospheric O₃ at WLG based on
80 EMAC model simulations using tagged tracers, revealing a peak contribution in June (Liu et al., 2020). At Nam Co station
81 (NMC) in the southern TP stratospheric influence was also mainly observed during spring and summer, which was estimated
82 to contribute 20% and 10%, respectively, based on model simulations (Yin et al., 2017). Measurements from Dangxiong, a
83 lower site not far from NMC, also revealed significant stratospheric impacts on surface O₃ (Lin et al., 2015). At Xianggelila
84 station in the southeastern TP, the STE impact was suggested to be most pronounced during winter and weakest during
85 spring and summer based on surface observations (Ma et al., 2014), which however was in disagreement with modelling
86 results revealing strongest STE during April and May, with an annual average contribution of 4.3%. In comparison, PAN
87 was far less investigated, the few existing studies mainly focused on the impact of transport on local PAN variations. Zhang
88 et al. (2009) made measurements of O₃ and PAN at WLG station during summer 2006 and found that the two oxidants
89 exhibited distinct diurnal variations and only weak correlations to each other, suggesting they were controlled by different
90 processes, with PAN being strongly influenced by regional transport of polluted air plumes. Xue et al. (2011) analyzed the
91 same set of observations and reported PAN to be one of the most abundant reactive nitrogen species (NO_y) at WLG,
92 contributing 32% to total NO_y. Xu et al. (2018b) made measurements of O₃ and PAN at NMC station in summer 2011 and
93 late spring to early summer 2012, detecting highly similar diurnal variations in both gases caused by boundary layer
94 development and elevated PAN in connection with transport of air plumes crossing over Nepal, North Pakistan or North
95 India.

96 Despite the findings in previous literature, the physicochemical factors determining the variation of O₃ and PAN in the TP
97 and their relative contributions have not been comprehensively investigated mainly due to the lack of comprehensive online
98 VOCs observations and accurate NO_x measurements. In this study, we present integrated real-time measurements of
99 O₃, PAN, NO₂, VOCs, CH₄, CO, photolysis rates and other meteorological parameters during spring and summer 2019 at
100 NMC station and analyzed them in combination with reanalysis data, utilizing trajectory modelling and box-modelling

101 approaches. The different impact of distinct transport processes and photochemical formation on O₃ and PAN, as well as
102 differences in sensitivities towards their precursors are intercompared using improved box-model constraints and the relative
103 contributions of physical and chemical processes to O₃ and PAN variability are evaluated.

104 **2 Experimental and analysis methods**

105 **2.1 Site, observations and data**

106 As the first part of the @Tibet series campaign, a campaign was carried out at NMC Station (30.77° N, 90. 95° E, 4730m
107 a.s.l.), which is a highly pristine site in the southern TP (Fig. 1). The site campus is located within the natural reserve of
108 NMC Lake, thus far away from anthropogenic activities and emissions. The nearest county (Dangxiong) and city (Lhasa) are
109 located 40 and 125 km to the southeast of NMC, respectively. The NMC Lake was ~1 km north to our observation site,
110 while the foothills of the northern Nyainqêntanglha Mountains were ~15 km to the south.

111 Measurements were performed from 1 May to 31 July 2019. Instruments for gases (including O₃, PAN, NO₂, CO, CH₄ and
112 non-methane volatile organic compounds (NMVOCs)) were housed in an air-conditioned container. O₃ was measured
113 alternately at the heights of 1.8 and 6.8 m (switching between two heights at 15-minute intervals) using a Model TE-49C
114 commercial O₃ analyzer, which was calibrated with a TE-49iPS O₃ calibrator (both from Thermo Electronics, USA). A Los
115 Gatos Research (LGR) NO₂ Analyzer was adopted for the measurements of NO₂, which has a measurement range of 0.01-
116 1000 ppb and was calibrated using NO₂ standard gas at the beginning and end of the experiment. PAN measurements were
117 made using a GC-ECD analyzer (Meteorologie Consult GmbH, Germany) which was calibrated using PAN instantly formed
118 in the reaction of a NO reference gas with acetone in the internal calibration unit of the instrument. CO and CH₄ were
119 measured (until 2 July) by a cavity ring-down spectroscopy (CRDS) analyzer (Model G2401, PICARRO, USA) at a high
120 precision (0.4 and 0.04 ppb, respectively, for CO and CH₄). The CRDS instrument was calibrated twice using a mixed CO
121 and CH₄ standard gas, which was pressurized in 29.5 L treated aluminum alloy cylinders (Scott-Marrin Inc.) fitted with high-
122 purity, two-stage gas regulators, and calibrated with cylinders assigned by the Global Atmosphere Watch (GAW) CO
123 Central Calibration Laboratory operated by National Oceanic and Atmospheric Administration (NOAA) Earth System
124 Research Laboratory (ESRL). NMVOCs were measured (only from 29 April to 21 May) using an online GC-MS/FID
125 analysis system (TH-PKU 300B, Wuhan Tianhong Instrument Co. Ltd., China) at a 1-hour time resolution, with detection
126 limits in the range of 0.004 to 0.066 ppb. Multipoint calibrations were performed using Photochemical Assessment
127 Monitoring Stations (PAMS) standard mixture and TO-15 standard mixture (100 ppb, Spectra Gases Inc., New Jersey, USA).
128 To account for the reactivity of different VOCs species, Propy-Equivalent VOCs concentrations were calculated as:

$$129 \quad C_{Propy-Equiv}(i) = C(i) \frac{k_{OH}(i)}{k_{OH}(C_3H_6)}, \quad \text{Eq. (1)}$$

130 where $C(i)$ is the ppbC concentration of species i (calculated using ppb mixing ratios multiplied by carbon numbers of
 131 species i), $k_{OH}(i)$ the reaction rate of species i with OH radicals (obtained from master chemical mechanism,
 132 <http://mcm.york.ac.uk/MCM/>), and $k_{OH}(C_3H_6)$ the reaction rate of propene with OH.
 133 Photolysis rates (J values) were obtained using a Metcon CCD-spectrograph (Meteorologie consult GmbH, Germany),
 134 whose receptor optics were mounted on top of the container at the height of 2 m. Conventional meteorological parameters
 135 including temperature (T), relative humidity (RH), surface pressure (P), wind speed (WS) and wind direction (WD) were
 136 recorded by an Automatic Weather Station. In addition, meteorological reanalysis data (ERA5) from the European Centre for
 137 Medium-Range Weather Forecasts (ECMWF) were used for complimentary analysis.

138 2.2 Backward trajectory analysis and PSCF calculations

139 The HYSPLIT model (version 5) from NOAA Air Resources Laboratory (Draxler and Hess, 1997; Draxler and Hess,
 140 1998; Draxler, 1999) was used for backward trajectory calculations, with 0.25° resolution GFS data from the National Center
 141 for Environmental Prediction (NCEP) adopted as input. The trajectory endpoint was set at 250 m above the ground level of
 142 NMC station. 7-day (168 hours) backward trajectories were calculated at an hourly interval for the entire period of the
 143 campaign.

144 The potential sources of high O_3 and PAN were studied using the potential source contribution function (PSCF) analysis,
 145 which has been widely applied to detect possible source regions (Ara Begum et al., 2005; Lucey et al., 2001; Zhou et al.,
 146 2004). The PSCF on grid (i,j) is defined as:

$$147 \text{PSCF} = m(i,j)/n(i,j), \quad (1)$$

148 where $m(i,j)$ is the residence time of a subset of trajectories, whereas $n(i,j)$ is the residence time of all the trajectories in that
 149 grid. Each trajectory was associated with O_3 and PAN concentrations observed at its time of arrival. To pin out the potential
 150 source regions for high O_3 and PAN, the $m(i,j)$ was calculated using the subset of trajectories that were associated with O_3 or
 151 PAN concentrations higher than their respective 75th percentiles.

152 Abnormally high PSCF values may be produced for certain grids with very small $n(i,j)$ values, which would induce large
 153 uncertainties. Thus, a weighting factor $W(n_{ij})$ is introduced that was proposed by Zeng and Hopke (1989), giving grids with
 154 few trajectories passing through less weight:

$$155 W(n_{ij}) = \begin{cases} 1.0, & n_{ij} > \bar{n}_{ij} \\ 0.7, & 0.1 \cdot \bar{n}_{ij} < n_{ij} \leq \bar{n}_{ij} \\ 0.4, & 0.05 \cdot \bar{n}_{ij} < n_{ij} \leq 0.1 \cdot \bar{n}_{ij} \\ 0.2, & n_{ij} \geq 0.05 \cdot \bar{n}_{ij} \end{cases}, \quad (2)$$

156 where \bar{n}_{ij} is the average number of n_{ij} .

157 The PSCF analysis was respectively performed for O_3 and PAN, separately for spring and summer periods. Based on
 158 meteorological variations, spring and summer periods were defined as 1 May to 15 June and 15 June to 31 July, respectively.

159

160 **2.3 Box modelling of local photochemistry**

161 The Master Chemical Mechanism (version 3.2) was used within the F0AM (version 3.1) box-model framework developed
162 by Wolfe et al. (2016), to simulate the impacts of local photochemistry on O₃ and PAN and to evaluate how much of their
163 variations could be explained through local photochemistry. Observation data of VOCs, NO₂, J values and meteorological
164 parameters were either averaged or interpolated into 10-minute averages and used as constraints in the model. Model
165 simulations were only performed for the period from 1 to 21 May, when VOCs observation data were available. To evaluate
166 local O₃ and PAN formation, three sets of simulations were performed for each, respectively using measurement constraints
167 on OVOCs, NO₂ or both of them. In O₃ simulation cases, PAN was constrained by observations, while in PAN simulations
168 O₃ was constrained. Daytime O₃ and PAN increments ($\Delta O_{3,mod}$ and ΔPAN_{mod}) were calculated and compared against
169 observed ones ($\Delta O_{3,obs}$ and ΔPAN_{obs}), with their ratios used to reflect how much modelled local photochemistry can explain
170 observed daytime increases in O₃ and PAN. Simulated O₃ and PAN net formation rates in distinct modelling scenarios were
171 intercompared and to evaluated the sensitivity of their formation to VOCs and NO_x concentrations.

172

173 **2.4 Impact of stratospheric-tropospheric exchange**

174 A Y index was defined as the ratio between normalized O₃ and water vapor concentrations, calculated using the following
175 equation:

$$176 Y_{ind} = \frac{O_3/\bar{O}_3}{H_2O/\bar{H}_2O}. \quad \text{Eq. (3)}$$

177 The Y index adopted in previous studies for the identification of stratospheric air intrusions has additionally divided Eq. (3)
178 by normalized CO concentrations (Ma et al., 2014). Due to the lack of CO measurements after 2 July, the Y index was
179 modified to the current form (in Eq. 3), which compared well with those calculated when incorporating normalized CO
180 concentrations (Fig. S1), since CO revealed very small variability during the entire observation period.

181 Additionally, O₃ mass mixing ratios from the ERA5 hourly reanalysis dataset were converted to volume mixing ratios and
182 applied in the investigation of STE impacts, since the ERA5 data are simulated with simple stratospheric O₃ chemistry
183 consideration and thus mainly represents the physical transport of stratospheric O₃ (Sprenger and Wernli, 2003).
184 Additionally, ERA5 O₃ data has been verified to be well representative of observed O₃ profiles and ground concentration
185 levels at remote polar regions (Wang et al., 2021), indicating that it can well represent stratospheric O₃ and the influence of
186 its transport.

187 **3 Results and discussions**

188 **3.1 Variational characteristics of O₃, PAN and their precursors**

189 The time series of observed O₃, PAN, NO₂, CO, photolysis rates of O₃ (jO¹D) and NO₂ (jNO₂), as well as meteorological
190 parameters observed at NMC from 1 May to 31 July are displayed in Figure 2. From 1 May to 15 June (defined hereafter as
191 the spring period), NMC experienced cold temperatures, strong winds, and dry conditions with low relative humidity (RH)
192 and hardly any precipitation except for three small snow events. While during 15 June to 31 July (defined hereafter as the
193 summer period), temperatures increased, average wind speeds were smaller and frequent precipitation events occurred under
194 the influence of the Asian summer monsoon (Fig. 2a, Table 1). Despite more frequent precipitation events, observed average
195 daytime photolysis rates were similar between spring and summer periods.

196 Under such meteorological variations, O₃ and PAN exhibited higher average concentrations in the spring (59.8±13.4 and
197 0.27±0.08 ppb) and lower ones in the summer period (53.6±13.2 and 0.20±0.05 ppb), with O₃ levels being overall in
198 accordance with previous observations (Xu et al., 2018b; Yin et al., 2017), while PAN levels were significantly lower than
199 those observed in 2012 (Xu et al., 2018b). VOCs concentrations were only obtained for the first half of the spring period,
200 reaching average concentrations of 4.9±3.3 Propy-Equiv. ppbC (10.5±3.2 ppb), to which OVOCs contributed 61±12%
201 (reaching 2.5±2.2 Propy-Equiv. ppbC on average), followed by alkenes (0.6±0.6 Propy-Equiv. ppbC), aromatics (0.6±1.3
202 Propy-Equiv. ppbC) and alkanes (0.5±0.5 Propy-Equiv. ppbC), which made up similar fractions (14±6%, 13±7%, and
203 11±4%, respectively), while other components (including alkynes, halogenated VOCs and nitriles) had negligible impacts
204 (1±1%) on the overall VOC concentration and reactivity (Fig. S2). Alkanes, alkenes and aromatics observed at the Dinghu
205 mountain (1000 m a.s.l.) background site in southern China were 48, 40 and 29 times of those observed at the Nam Co site
206 (Wu et al., 2016). Those in the Rocky Mountain National Park (3498 m a.s.l.) were 1.2, 3.6 and 1.3 times of those observed
207 in this study (Benedict et al., 2019), while those observed during summertime (1994-1996) were 0.9, 14 and 1.6 times of that
208 those in Nam Co (Ma et al., 2002), revealing the extremely low primary VOCs emissions at our site. However, OVOCs
209 concentrations at Nam Co were 1.3 times of those observed in the Rocky Mountains, while only 0.24 times of those
210 previously observed at Mt. Waliguan (Mu et al., 2007), indicating that air masses in the TP were strongly photochemically
211 aged due to the strong radiation and high atmospheric oxidative capacity at high altitudes, with additional influences from
212 natural sources such as plant emissions or animal excrement (mostly from yak and sheep). At Nam Co, concentrations of
213 isoprene and its oxidation products (e.g. MVK and MACR) were very low (0.034 ppb in total), with OVOCs being mostly
214 dominated by formaldehyde, acetaldehyde and acetone (3.2 ppb in total), which have shown elevated concentrations over
215 animal excrement (Mu et al., 2007). While daytime concentrations of OVOCs and alkenes were significantly higher than
216 those during nighttime, other VOCs species did not display much day-night discrepancy.

217 NO₂ revealed averaged concentrations 0.12±0.05 and 0.09±0.05 ppb during spring and summer periods, respectively, with
218 no evident day to night differences. NO_x levels were only scarcely reported for remote high-altitude locations, mainly due to
219 instrument limitations. NO₂ levels were only slightly higher than the average NO₂ and NO level reported at Mt. Waliguan

220 during summer 1994-1996 (0.048 ± 0.017 ppb) based on filter-pack sampling and spring 2003 (0.043 ± 0.069 ppb) based on
221 chemiluminescence (Ma et al., 2002; Wang et al., 2006). Since Nam Co is located far away from anthropogenic emission
222 sources, NO_x levels here are mainly determined by natural emissions, such as those from soil microbial activities or lightning
223 processes. Additionally, a latest study has proposed that lakes in the TP are strong NO_x emission sources of NO_x (Kong et al.,
224 2022). Averaged diurnal variations of O_3 and PAN resembled each other (Figs. 3a1-2), both revealing decreases after sunset,
225 reaching daily minimum concentrations near 7:00 Beijing Local Time (LT) and increasing quickly after sunrise simultaneous
226 to PBL height (PBLH, Figs. 3b1-2) and exhibiting a flat plateau afterwards. Daily minimum O_3 concentrations were
227 52.8 ± 10.9 and 48.3 ± 12.8 ppb, while those of PAN were 0.21 ± 0.06 and 0.17 ± 0.04 ppb during spring and summer,
228 respectively. Daily maximum O_3 reached 74.3 ± 6.7 and 63.5 ± 13.0 ppb, while those of PAN reached 0.31 ± 0.08 and
229 0.22 ± 0.06 ppb during spring and summer, respectively. Thus, O_3 and PAN both revealed higher levels in spring and lower
230 ones in summer, however, PAN concentrations have decreased more significantly than O_3 (26% versus 10%), revealing a
231 very flat and broad plateau during the day. OVOCs, aromatics and alkenes determined the variations of VOCs, with OVOCs
232 and alkenes displaying diel variations similar to those of O_3 and PAN, revealing increases from 7:00 to 9:00 LT, fluctuating
233 around its daily maximum value over daytime and decreasing after 17:00 LT (Figs. 3b1-2). NO_2 was typically higher during
234 nighttime and lower during daytime, which is caused by combined effects of weakened dilution under nighttime shallow
235 boundary layers, natural and anthropogenic NO_x emissions, as well as chemical transformations. Additionally, springtime
236 NO_2 concentrations (0.12 ± 0.04 ppb) were higher than those during the summer period (0.09 ± 0.05 ppb, Figs. 3c1-2). CO,
237 however, revealed only slightly higher concentrations during the summer period (107 ± 26 and 117 ± 29 ppb in spring and
238 summer, respectively), staying overall flat during the day, without any diurnal variations (Figs. 3c1-2). Both RH and
239 absolute water vapor concentrations were higher during the summer period. RH revealed a diurnal maximum by 7:00 LT
240 during both periods, decreased rapidly after sunrise and reached its diurnal minimum at 16:00 and 18:00 LT in spring and
241 summer, respectively (Fig. 3e1-2). Water vapor, however, increased further after sunrise, possibly due to surface evaporation
242 processes of frost and dew during the morning. While the diurnal peak in photolysis rates were similar between spring and
243 summer periods, the averaged diurnal variations displayed a narrower peak during summer, especially for $j\text{NO}_2$, due to more
244 frequent precipitation and higher cloud coverage.

245 The day-to-day evolution of diurnal O_3 and PAN variations as well as those of winds and PBLH are more clearly displayed
246 by Figs. 4). Downward winds were strongest during the afternoon under high PBLH (Figs. 4a,d). Due to the local
247 topography with the NMC Lake to its west and north and the Nyainqêntanglha Mountains to its south, the site was
248 susceptible to both influences from land-lake and mountain-valley breezes. Accordingly, local surface winds displayed clear
249 diurnal variations with southeasterly nighttime winds shifting to northwesterly winds during daytime (Figs. S3b-d, Fig. S3 is
250 the same as Fig. 4, with winds replaced by 2 m wind measurements). 550 hPa winds from ERA5 over the 0.25° grid
251 containing NMC station (representing near surface conditions, since surface pressure was on average 573 ± 2 hPa) revealed
252 stronger diurnal variations in zonal winds (Fig. 4b), overall agreeing with variations in surface winds, while meridional

253 winds were dominated by southerly wind directions (Fig. 4c), with occasional changes to northerly winds, suggesting that
254 local circulations had stronger impacts on zonal winds.

255 Broad peaks in O₃ often lasted until late evening hours, while nighttime O₃ frequently revealed increases under westerly
256 winds and could reach daytime concentration levels, which can only be attributed to transport processes. High nighttime O₃
257 was not always accompanied by simultaneous PAN increases, while vice versa, elevated nighttime PAN was also not always
258 synchronized with those of O₃, indicating that they might have originated from distinct sources and processes. O₃ levels were
259 continuously high throughout the spring period, especially during 6-13 May. Despite overall lower levels in the summer
260 period, two O₃ episodes occurred during 7-8 July and 24-25 July, respectively, exhibiting the highest concentrations (daily
261 maximum concentrations ranging from 85.9 to 91.9 ppb) observed during the entire campaign (Fig. 2a, Fig. 4e). Compared
262 to O₃, PAN displayed much larger day to day variability, with an evident high PAN episode occurring from 13 to 16 May
263 (0.42 ± 0.08 ppb on average) under southeasterly winds from aloft (Fig. 4f). Summertime PAN was distinctly lower than that
264 during spring season, with no increases detected during the two high O₃ episodes.

265 Overall, while O₃ and PAN revealed highly similar average diurnal variation patterns, their temporal variations often differed
266 from each other, suggesting that they were determined by distinct transport or formation processes, which will be further
267 investigated in the following sections.

268

269 **3.2 Impact of local circulation**

270 In previous studies, diurnal variations in O₃ and PAN were mainly attributed to local circulations, particularly the
271 development of the PBL. At pristine mountain sites such as WLG, surface O₃ was influenced by free tropospheric air during
272 nighttime and by boundary layer air masses during daytime, which resulted in a diurnal cycle with lower daytime and higher
273 nighttime O₃ with very small diurnal variation amplitudes. Despite its high altitudes, NMC is located at the foot of the
274 northern Nyainqêntanglha Mountains, and thus experienced local circulation distinct from those at WLG. Free tropospheric
275 air was suggested to be richer in O₃ and PAN concentrations and was mixed down upon the rapid development of the
276 convective boundary layer (CBL) after sunrise, while O₃ and PAN concentrations decreased upon the establishment of the
277 nocturnal boundary layer (NBL), due to the dominance of local boundary layer air masses during nighttime, which were low
278 in O₃ and PAN, since barely any surface O₃ and PAN precursor emission sources existed at NMC, added by effects of dry
279 deposition (Xu et al., 2018b). The broad O₃ peaks that often lasted until late evenings and the frequent events of elevated
280 nighttime O₃ (occurrence frequency of 38%, Fig. 4e) both supported the idea that under favorable meteorological conditions,
281 high surface O₃ levels after sunlight hours could be sustained by continuous downmixing of free tropospheric air (average
282 daily maximum nighttime O₃ reaching 67.6 ± 10.1 and 62.9 ± 6.4 ppb during spring and summer, respectively). The fact that
283 nighttime O₃ could reach the same level as noontime O₃ is why previous studies suggested that physical transport was
284 determining O₃ variations at NMC, while photochemistry played a minor role.

285 Diurnal variations of O₃ and PAN followed their averaged diel pattern on 72% and 75% out of the days with valid records,
286 respectively. While O₃ diurnal cycles revealed more days with such daytime increases during summer (69% in spring vs. 74%

287 in summer), PAN conformed better to its averaged diurnal cycle in spring (90% in spring vs. 63% in summer), suggesting
288 that despite being under the same meteorological influences and despite highly similar average diurnal concentration profiles,
289 O₃ and PAN often revealed different variations. O₃ and PAN increasing rates (on days with daytime increases) between 7:30
290 and 10:30 LT both displayed linear correlations to temperature increasing rates ($r=0.45$ and 0.52 for O₃ and PAN,
291 respectively, Fig. S4), confirming again that their morning increases were closely connected to boundary layer development
292 upon radiative heating. Prenoon (6:00 to 12:00 LT) O₃ concentrations also increased with PBLH during both spring (Fig. 5a)
293 and summer (Fig. 5b), however, revealing slightly distinct slopes during distinct seasons. Weaker prenoon winds that mainly
294 occurred during early morning under low PBLH conditions were associated with evidently lower O₃ concentrations. During
295 early morning hours when PBLH was still low, strong winds that mostly came from the W-NW direction were associated
296 with O₃ concentrations as high as those observed during noontime in the spring period (Fig. 5a). During the afternoon (12:00
297 to 18:00 LT), when the CBL has fully established, O₃ hardly displayed any more variation with PBLH (Fig. S5a), indicating
298 that once boundary layer and free tropospheric air was fully mixed, O₃ did not further increase with PBLH. In the summer
299 period, W-NW winds were less frequent and O₃ associated with these winds only increased weakly with PBLH, whereas N-
300 NE winds resulted in more significant rise in O₃ over prenoon hours. Summertime afternoon PBLH was significantly lower
301 than during spring due to frequent cloudy and rainy conditions, mostly falling into the range of 0.5-1.5 km (Fig. S5b). O₃ still
302 increased with PBLH, however, revealing large variability under the same PBLH, indicating that PBLH was not the
303 deterministic factor for afternoon O₃ levels. PAN did not replicate the variation of O₃ with PBLH during prenoon hours,
304 displaying large variability at lower PBLH and moderate concentration levels under high PBLH. This suggests that free
305 tropospheric O₃ levels were consistently and significantly higher than boundary layer O₃ levels, indicating for weak surface
306 formation of O₃ (further discussed in Sect. 3.3), which resulted in significant increases in observed surface O₃ upon down
307 mixing. Whereas free tropospheric PAN or the surface formation of PAN might have had higher variability, which resulted
308 in largely different responses of PAN with the down mixing of free tropospheric air. Intensive downmixing for free
309 tropospheric air under high PBLH might have even diluted boundary layer PAN concentrations.

310 To investigate what has caused the discrepancies in free tropospheric O₃ and PAN over NMC, the variations of surface O₃
311 and PAN with free tropospheric (500-550 hPa) winds during spring and summer are depicted in Fig. 6. At lower wind speeds,
312 both O₃ and PAN typically revealed lower concentrations. With increasing wind speeds, high concentrations of O₃ and PAN
313 were associated with distinct wind directions, in both spring and summer. During springtime, high concentrations of O₃ and
314 PAN both occurred with W winds, however, low O₃ and high PAN concentrations were detected under strong S winds.
315 During summertime, high O₃ dominantly occurred with N-NE winds, while PAN mainly revealed elevated concentrations
316 under S-SW winds. The distinct variation of O₃ and PAN with wind speed and wind direction suggests that the
317 concentrations of both gases might have been impacted by different long-range transport processes, which will be
318 investigated in the next section.

319

320 **3.3 Impact of inter-regional transport and stratospheric-tropospheric exchange**

321 Potential influence of pollution transport from India and other south Asian countries have been previously reported, which
322 had potential impacts on the transport of PAN (Xu et al., 2018b). However, the source regions of O₃ and PAN in the TP have
323 not been systematically investigated before. NO₂ and CO columns from TROPOMI revealed high concentrations in South
324 Asian regions south of the TP contrasting to the pristine environment within the TP (Fig. 7). CO was more severe and
325 widespread outside of the TP during the spring period, while NO₂ pollution was more severe during the summer period both
326 in South Asia and to the east of the TP in China. Inside the TP, NO₂ and CO columns were both higher during the summer
327 period, suggesting that summertime atmospheric circulations might have been more favorable for pollution transport into the
328 TP. The high-altitude Himalaya mountains along the southern border of the TP is highly effective in blocking out direct
329 intrusion of South Asian pollution, leading mostly to pollutant accumulation on its southern slope. High resolution satellite
330 observations clearly reveal high NO₂ and CO along mountain and river valleys, indicating that pollution might have
331 transported into the TP through these passageways. Belts of elevated CO extend from the western side (Kashmir) to the
332 southeastern corner of the TP, indicating that pollution from South Asia could not directly cross over the Himalayas,
333 especially not over those regions with very high altitudes, but had entered the TP by crossing either to its west or southeast.
334 To further identify possible source regions for high O₃ and PAN at NMC station, the PSCF for both gases were calculated
335 for spring and summer, respectively (Fig. 8). Spring time high O₃ concentrations were mainly associated with westerly
336 trajectories, which crossed over North India and Nepal before arriving at NMC (Fig. 8a). Although trajectories associated
337 with high springtime O₃ crossed over vast areas outside the southern TP border, they mainly entered the TP from two
338 passageways, one from the west and another from the southeast (near the border of Bhutan). Before entering the TP, the
339 majority of the air masses associated with high O₃ came from higher altitudes (> 6 km), diving downwards to heights of 3-
340 6 km or even < 3 km near the southern border of the TP, and then entering the TP mainly from the west or south (Figs. 9a1-
341 3). Aside from that, trajectories from the NW mostly travelling within 0-6 km (above ground level) were also associated
342 with high springtime O₃. High springtime PAN, however, was only associated with trajectories crossing over South Asia and
343 entering the TP from the southeastern border. In addition, air masses from the Indian Ocean that travelled within 0-3 km and
344 crossed over Bangladesh and Bhutan were also associated with high PAN, while not with high O₃ (Fig. 8b and Figs. 9b1-3).
345 During summer, the PSCF of O₃ revealed a largely different distribution from that in spring. High altitude westerly air
346 masses that entered the TP from the west in spring have not been seen in summer, while air masses sweeping along the
347 southern border of the TP (Nepal and northern India) at altitudes below 6 km and approaching NMC from its south were still
348 partly associated with high O₃ during summer (Fig. 8c and Figs. 9c1-3). Southerly low altitude (0-3 km) maritime air masses
349 that travelled over Bangladesh and Bhutan before entering the TP were also sometimes linked to high O₃ at NMC. However,
350 the major summertime O₃ source regions were located to the north of NMC, including southern Xinjiang province, Northern
351 Tibet and western Qinghai Province (Fig. 8c). High O₃ was mostly associated with low altitude air masses from the NW and
352 N directions (Fig. 9c1). Summertime PAN was only rarely associated with northerly air masses, but mostly linked to
353 westerly trajectories that travel along the southern TP border (mostly within 0-3 km, small parts within 3-6 km altitude, Figs.
354 9d1-2) and southerly trajectories travelling over Bangladesh and Bhutan within 3 km altitude (Fig. 9d1).

355 Thus, O₃ and PAN revealed distinct source regions in both spring and summer, while they also shared some common source
356 regions. This explains why despite highly similar diel variation patterns, the day-to-day variation was often different between
357 the two photochemical pollutants. Overall, springtime synoptic conditions resulted in a relatively monotone origin of air
358 masses at NMC, mostly favoring the subsidence of high altitude air masses under westerly airflows, which were rich in both
359 O₃ and PAN. With the onset of the South and East Asian Monsoon during summer, circulations drastically changed and
360 resulted in influences of various distinct air mass origins at NMC. These vastly different air mass origins also exhibited
361 completely different O₃ levels, with those originated in the north exhibiting even higher O₃ levels than those observed during
362 springtime and southerly air masses revealing much lower O₃ levels than during springtime. PAN, however, was more linked
363 to westerly and southerly air masses during summer.

364 Aside from changes in air mass origins at NMC, seasonal variations in large scale synoptic conditions were also
365 deterministic of STE and the overall spatial distribution of O₃. Since the ERA5 reanalysis data has only considered
366 simplified stratospheric O₃ chemistry and the physical transport of O₃, the O₃ mixing ratio in the ERA5 dataset is a good
367 indicator for the investigation of stratospheric influences. During the spring period, the averaged ERA5 500 hPa O₃ revealed
368 relatively lower mixing ratios in the TP region (especially in southeast TP) and higher mixing ratios outside the TP in the
369 latitude band between 15 and 25°N. As was shown in previous studies, the downward transport of stratospheric O₃ and its
370 distribution is closely linked to the location of the subtropical jet stream (Xu et al., 2018a), which is typically located above
371 the TP during the spring period (Fig. 10c1). Due to large scale circulations, lower stratospheric O₃ is typically high in polar
372 regions, decreasing with latitude and reaching its lowest level in the equatorial belt (Fig. 10c1). Deep stratospheric intrusion
373 and O₃ subsidence often occur along the lower edge of the subtropical jet stream, which is a slope extending from the lower
374 stratosphere (150 hPa) between 38 to 42°N down to the middle or upper troposphere below 28°N. STE processes are
375 especially promoted by fronts, which are accompanied by large scale subsidence of cold air from above (Stohl et al., 2003).
376 STE mostly increased the O₃ levels in Southeast Asia to the west and south of the TP, which in turn could enhance O₃ at
377 NMC through the westerly air mass transport passage (Figs. S6). Direct STE influence was also frequently observed during
378 the spring period (on 5-8, 13, 23, 31 May and 3, 5 and 9 Jun, Figs. S7-13), with NMC frequently located near low pressure
379 troughs behind cold fronts. These STE events were typically associated with high O₃ and low PAN concentrations, except
380 for the 13 May, when stratospheric O₃ was transported to lower latitudes and then back to NMC via southwesterly winds,
381 which also carried along high PAN concentrations, suggesting that NMC experienced aged stratospheric air masses. During
382 the summer period, with the northward shift of the subtropical jet stream, the high lower stratospheric O₃ concentrations
383 were also confined within higher latitudes. 500 hPa ERA5 O₃ revealed a clearly distinct distribution from that during spring,
384 displaying higher O₃ levels north of NMC (>30 °N) and much lower ones in the tropical region. Thus, under the prevailing
385 southerly winds during the summer season, air masses with lower stratospheric O₃ contents are transported to NMC.
386 However, during two episodes on 7-9 and 21-25 Jul, northerly cold air masses in front of 500 hPa high pressure systems over
387 the TP brought stratospheric O₃ down to the norther TP regions and transported them within lower altitudes to NMC,

388 resulting in surface O₃ levels even higher than those during springtime (Figs. S14-15), while PAN did not reveal significant
389 increases.

390 Statistically, O_{3,ERA5} only explained 0.1% of the observed daytime O₃ day-to-day variability during spring ($r=0.033$),
391 however, explained 22% of the summertime O_{3,NMC} variability ($r=0.47$), contributing on average 10% during the entire
392 observation period (Fig. S16), which was overall in accordance with previous results reported in Yin et al. (2017). It is also
393 worth noting that observed O₃ at NMC was typically higher than the 550 hPa ERA5 O₃ mixing ratio, especially during spring
394 and early summer (Fig. 10d). During the entire observation, stratospheric O₃ transport explained 83% of the observed
395 daytime O₃ concentration ($O_{3,ERA5}/O_{3,NMC}$), with a lower contribution during spring (77%) and a higher one during summer
396 (88%). This suggests that despite the small contributions of STE to the day-to-day variability of observed O₃, the overall
397 daytime O₃ concentration was mainly maintained by the long-range transport of stratospheric O₃ (as opposed to direct strike
398 of stratospheric O₃ during deep STE intrusions into the PBL). Additionally, the unexplained O₃ concentration might indicate
399 for photochemical O₃ formation aside from pure physical transport. However, whether it was caused by local photochemical
400 production or the long-range transport of photochemically produced O₃ still requires further investigation.

401

402 **3.4 Impact of local photochemistry**

403 As was already manifested, O₃ has its natural sources and is more affected by STE processes at high altitude locations such
404 as NMC. O₃ is highly reactive and can be easily depleted in regions with high NO_x and VOCs emissions, however has a
405 relatively longer lifetime in pristine background areas and can be directly or indirectly transported (transport of its precursors)
406 over large distances, affecting O₃ levels at remote locations (Xu et al., 2018a). The impact of local photochemistry on the
407 budget of O₃, however, was often under debate in previous studies conducted in background areas of the TP. Under such
408 pristine atmospheric conditions, it was manifested that O₃ production was strongly NO_x-limited, with NO_x concentrations
409 being the key factor determining whether O₃ was net produced or destructed in local photochemistry (Ma et al., 2002).
410 However, the lower detection limit and precision of commercial instruments can hardly meet the needs for NO_x
411 measurements in such clean environments, which made it difficult to determine whether there has been net O₃ formation. At
412 higher altitudes, PAN has a long lifetime and can be transported over long distances. PAN measurements have been
413 previously conducted at Mt. Waliguan (Northeastern TP) in 2006 (Xue et al., 2011) and at NMC station in the springs and
414 summers of 2011 and 2012 (Xu et al., 2018b). At both sites, PAN contributed substantially to reactive nitrogen and acted as
415 a good indicator for regional and long-range transport of polluted air plumes. The photochemical formation of PAN requires
416 the presence of peroxy acetyl radical and NO₂. The former is only formed in photochemical reactions of its precursor
417 OVOCs, which are predominantly emitted within the boundary layer, while the latter is also mostly emitted near surface,
418 with the exception of lightning processes. Overall, the formation of PAN in comparison with O₃ is more likely to occur near
419 surface and has no natural sources. Nevertheless, the impact of local PAN formation versus those of transport to observed
420 concentration levels was not discussed before due to the lack of its precursor measurements.

421 To evaluate the contribution of local photochemistry to observed O₃ and PAN, simulations were performed using an MCM-
422 based box model for the period of 1 to 21 May, when VOCs measurements were available. Observed O₃ revealed much
423 larger fluctuations than those obtained from all three simulation scenarios, which respectively used measurement constraints
424 on OVOCs, NO₂ or both of them (Fig. 11a). With constraints on NO₂, modelling results revealed significant daytime
425 increases, indicating positive local net photochemical formation of O₃ (Fig. 12a). However, when NO₂ was unconstrained,
426 modelled O₃ concentrations were significantly lower and displayed very small variability, with very small positive net O₃
427 production during the morning and mostly negative ones during the day (Fig. 12a). Nevertheless, none of the simulations
428 could account for the large variability and steep morning increases within observed O₃, with OVOCs and NO₂ both
429 constrained by measurements, modelling results could only explain 28±19% (5-66%) of the observed daytime increases (Fig.
430 11b), while even less could be explained when only OVOCs or NO₂ was constrained (3±6% and 21±14%, respectively).
431 Days with relatively stronger local photochemical O₃ formation were not necessary days with high observed O₃. In turn, days
432 with high O₃ were also often associated with weak photochemical net O₃ formation. This indicates that physical transport
433 and mixing processes were determinative of O₃ diel cycle as well as the day-to-day O₃ variability, while local
434 photochemistry further added to the daytime O₃ burden. Additionally, intercomparison among simulations also confirmed
435 the high sensitivity of O₃ formation towards NO_x and the relatively weaker sensitivity to VOCs in such a pristine
436 environment.

437 Simulated PAN levels under NO₂ constraints were, however, significantly higher than observed PAN concentrations,
438 especially when OVOCs and NO₂ were both constrained. However, when NO₂ was unconstrained, PAN concentrations were
439 mostly underestimated by simulations. Thermal decomposition of PAN was very weak under low springtime temperatures
440 and net photochemical PAN formation rates were positive under all simulation scenarios, however, only NO₂ constrained
441 cases revealed strong formation throughout daytime hours (08:00-20:00 LT) while unconstrained NO₂ simulations only
442 displayed a very weak morning time (07:00-9:00 LT) photochemical formation. Only NO₂-constrained simulations
443 overestimated PAN concentrations by a factor of 1.8 on average, however, could reproduce observed daytime PAN
444 increments by 94±84%. Additionally, days with high simulated PAN photochemical production (4-6 and 13-17 May)
445 corresponded to episodes with elevated observed PAN concentrations, which indicates that photochemical formation of PAN
446 were determinative of its day-to-day variability. Compared to O₃, PAN was sensitive to concentrations of both OVOCs and
447 NO₂, since some of the OVOCs are direct precursors of PA radicals, which combine with NO₂ in PAN formation. According
448 to modelling results in Fig. S17, acetaldehyde oxidation contributed majorly to PA radical formation at Nam Co (71.8%),
449 followed by methylglyoxal (9.0%) and biacetyl (5.1%). Still, NO₂ was more decisive of the overall O₃ and PAN production,
450 since without its constraint, O₃ net loss and negligible PAN net formation would be yielded.

451 It should also be noted that both observed O₃ and PAN were not necessarily formed within the local boundary layer, since
452 springtime winds in the TP were very strong, especially during daytime. Due to its relatively long lifetime, PAN might have
453 been formed on the transport pathway to NMC, while O₃ might undergo both destruction and production during airmass
454 transport. This might partly explain why PAN formation was overestimated by simulations representing surface conditions.

455 But overall, it could be concluded that O₃ was mainly determined by physical transport, particularly STE processes, while
456 PAN was largely determined by local photochemistry and that along the transport passageway. Fresh STE plumes reaching
457 NMC from the north where PAN concentrations result in depleted surface PAN, while relatively aged STE air masses
458 crossing over polluted regions of Indo-Gigantic Plain led to simultaneous enrichment in surface O₃ and PAN. The high
459 sensitivity of O₃ and PAN formation towards NO_x indicates that increased natural emission of NO_x under global warming,
460 enhanced anthropogenic emissions of NO_x within the TP region due to the development of highways and transportation as
461 well as increased transport input from South Asia might greatly enhance O₃ and PAN formation in background regions,
462 while increased VOCs emissions and regional transport promotes PAN formation more than that of O₃.

463

464 **4 Conclusions and implications**

465 In this study, continuous measurements of O₃ and PAN as well as its precursors were conducted during the spring and
466 summer season at a very pristine high-altitude site in the southern TP (NMC station) to investigate the factors determining
467 their variations. Due to the local topography, surface observations at NMC reflect free tropospheric air conditions during
468 daytime and nocturnal boundary layer conditions during nighttime. Both O₃ and PAN revealed steep increases after sunrise
469 and reached a flat plateau during daytime. While average diurnal variations of O₃ and PAN highly resembled each other,
470 their day-to-day variations were often different, suggesting that they might have been influenced by distinct physicochemical
471 processes.

472 Backward trajectory modelling and PSCF analysis revealed distinct source regions connected to high O₃ and PAN. During
473 spring, air masses rich in O₃ were mainly associated with high altitude westerly air masses that either entered the TP from
474 the west or from the south, while PAN was only rich in westerly air masses that transported along the polluted regions in
475 North India and Nepal before entering the TP from the south or in southerly air masses of maritime origin that crossed over
476 polluted South Asian regions before entering the TP. During the summer monsoon season, air masses from the north were
477 associated with the highest O₃ levels, while westerly and southerly air masses revealed lower O₃ levels. Elevated PAN
478 concentrations, however, were still linked to westerly and southerly air masses crossing over polluted South Asian regions.
479 O₃ at NMC was strongly influenced by STE, which brought down high stratospheric O₃ concentrations from the southwest
480 route during spring and from the northwest during summer, explaining 77% and 88% of the observed O₃ level in spring and
481 summer, respectively. PAN concentrations were, however, typically lower in air masses with strong stratospheric influence,
482 except if they transported over polluted regions south of the TP.

483 Photochemistry resulted in positive net formation of both O₃ and PAN. While only 28±19% of the observed daytime growth
484 in O₃ could be explained by photochemical simulations, the daytime growth of PAN was highly overestimated by the model
485 if OVOCs and NO₂ were both constrained. Photochemistry was not the factor determining the day-to-day variability of O₃,
486 however, explained observed PAN variabilities well. While both O₃ and PAN formation were highly sensitive to NO_x levels,
487 PAN was also quite sensitive to VOCs concentrations. Therefore, future concentrations of O₃ and PAN over the TP may be
488 significantly impacted by increases in the concentrations of NO_x, VOCs, and other precursors (Cui et al., 2016), which either

489 originate from the surrounding regions (in particular South Asia) or from anthropogenic and natural sources within the TP.
490 Special attention should be paid to PAN, which is mostly determined by photochemical processes sensitive to both NO_x and
491 VOCs and can be transported over very long distances.

492

493 **Data availability.** The data used in this study are available on the @Tibet ftp server (<http://at-tibet.quickconnect.cn/>) and
494 can be applied for upon request to the corresponding authors (zhanggen@cma.gov.cn and c.ye@pku.edu.cn)

495

496 **Author contributions.** WX and CY designed the experiment and led the research. WX, GZ, CY, YW, YZ, YB, WL, XX
497 were responsible for the maintenance of trace gas and meteorology measurements in the experiment and WX, YZ and YW
498 processed the data. WX analyzed the data and wrote the paper with help from XZ, XX and GZ.

499

500 **Competing interests.** The authors declare that they have no conflict of interest.

501

502 **Acknowledgments, Samples, and Data**

503 This work is supported by the National Natural Science Foundation of China (41875159, 42175127, 42275127, 42075112,
504 and 42105110) and the Natural Science Foundation of Beijing (8222078).

505

506 **References**

- 507 Ara Begum, B., Kim, E., Jeong, C.-H., Lee, D.-W., and Hopke, P. K.: Evaluation of the potential source contribution function using the
508 2002 Quebec forest fire episode, *Atmospheric Environment*, 39, 3719-3724, 10.1016/j.atmosenv.2005.03.008, 2005.
- 509 Benedict, K. B., Zhou, Y., Sive, B. C., Prenni, A. J., Gebhart, K. A., Fischer, E. V., Evanoski-Cole, A., Sullivan, A. P., Callahan, S.,
510 Schichtel, B. A., Mao, H., Zhou, Y., and Collett Jr, J. L.: Volatile organic compounds and ozone in Rocky Mountain National Park during
511 FRAPPÉ, *Atmos. Chem. Phys.*, 19, 499-521, 10.5194/acp-19-499-2019, 2019.
- 512 Cui, Y., Lin, J., Song, C., Liu, M., Yan, Y., Xu, Y., and Huang, B.: Rapid growth in nitrogen dioxide pollution over Western China, 2005–
513 2013, *Atmos. Chem. Phys.*, 16, 6207-6221, 10.5194/acp-16-6207-2016, 2016.
- 514 Ding, A., and Wang, T.: Influence of stratosphere-to-troposphere exchange on the seasonal cycle of surface ozone at Mount Waliguan in
515 western China, *Geophysical Research Letters*, 33, L03803, 10.1029/2005GL024760, 2006.
- 516 Draxler, R. R., and Hess, G. D.: Description of the HYSPLIT_4 modeling system, NOAA Tech. Memo, ERL ARL-224, NOAA Air
517 Resources Laboratory, Silver Spring, MD, 24 pp., 1997.
- 518 Draxler, R. R., and Hess, G. D.: An overview of the HYSPLIT_4 modelling system for trajectories, dispersion and deposition, *Australian*
519 *Meteorological Magazine*, 47, 295-308, 1998.
- 520 Draxler, R. R.: HYSPLIT4 user's guide, NOAA Tech. Memo, ERL ARL-230, NOAA Air Resources Laboratory, Silver Spring, MD, 1999.
- 521 Fischer, E. V., Jacob, D. J., Yantosca, R. M., Sulprizio, M. P., Millet, D. B., Mao, J., Paulot, F., Singh, H. B., Roiger, A., Ries, L., Talbot,
522 R. W., Dzepina, K., and Pandey Deolal, S.: Atmospheric peroxyacetyl nitrate (PAN): a global budget and source attribution, *Atmos. Chem.*
523 *Phys.*, 14, 2679-2698, 10.5194/acp-14-2679-2014, 2014.
- 524 Hu, B., Liu, T., Hong, Y., Xu, L., Li, M., Wu, X., Wang, H., Chen, J., and Chen, J.: Characteristics of peroxyacetyl nitrate (PAN) in a
525 coastal city of southeastern China: Photochemical mechanism and pollution process, *Science of The Total Environment*, 719, 137493,
526 <https://doi.org/10.1016/j.scitotenv.2020.137493>, 2020.
- 527 Kleindienst, T. E., Shepson, P. B., and Smith, D. F.: Comparison of mutagenic activities of several peroxyacyl nitrates, *Environmental and*
528 *molecular mutagenesis*, 16, 70-80, 1990.

529 Kong, H., Lin, J., Zhang, Y., Li, C., Xu, C., Shen, L., Liu, X., Yang, K., Su, H., and Xu, W.: Unexpected high NO_x emissions from lakes
530 on Tibetan Plateau under rapid warming, *Nature Geoscience* (Accepted), <https://doi.org/10.21203/rs.3.rs-1980236/v1>, 2022.

531 Langford, A. O.: Stratosphere-troposphere exchange at the subtropical jet: Contribution to the tropospheric ozone budget at midlatitudes,
532 *Geophysical Research Letters*, 26, 2449-2452, 10.1029/1999GL900556, 1999.

533 Lefohn, A. S., Malley, C. S., Simon, H., Wells, B., Xu, X., Zhang, L., and Wang, T.: Responses of human health and vegetation exposure
534 metrics to changes in ozone concentration distributions in the European Union, United States, and China, *Atmospheric Environment*, 152,
535 123-145, <https://doi.org/10.1016/j.atmosenv.2016.12.025>, 2017.

536 Lin, W., Xu, X., Zheng, X., Dawa, J., Baima, C., and Ma, J.: Two-year measurements of surface ozone at Dangxiong, a remote highland
537 site in the Tibetan Plateau, *Journal of Environmental Sciences*, 31, 133-145, <http://dx.doi.org/10.1016/j.jes.2014.10.022>, 2015.

538 Liu, L., Wang, X., Chen, J., Xue, L., Wang, W., Wen, L., Li, D., and Chen, T.: Understanding unusually high levels of peroxyacetyl nitrate
539 (PAN) in winter in Urban Jinan, China, *Journal of Environmental Sciences*, 71, 249-260, <https://doi.org/10.1016/j.jes.2018.05.015>, 2018.

540 Liu, N., Ma, J., Xu, W., Wang, Y., Pozzer, A., and Lelieveld, J.: A modeling study of the regional representativeness of surface ozone
541 variation at the WMO/GAW background stations in China, *Atmospheric Environment*, 242, 117672,
542 <https://doi.org/10.1016/j.atmosenv.2020.117672>, 2020.

543 Lucey, D., Hadjiiski, L., Hopke, P. K., Scudlark, J. R., and Church, T.: Identification of sources of pollutants in precipitation measured at
544 the mid-Atlantic US coast using potential source contribution function (PSCF), *Atmospheric Environment*, 35, 3979-3986, 10.1016/s1352-
545 2310(01)00185-6, 2001.

546 Ma, J., Tang, J., Zhou, X., and Zhang, X.: Estimates of the Chemical Budget for Ozone at Waliguan Observatory, *Journal of Atmospheric*
547 *Chemistry*, 41, 21-48, 10.1023/A:1013892308983, 2002.

548 Ma, J., Lin, W. L., Zheng, X. D., Xu, X. B., Li, Z., and Yang, L. L.: Influence of air mass downward transport on the variability of surface
549 ozone at Xianggelila Regional Atmosphere Background Station, southwest China, *Atmospheric Chemistry and Physics*, 14, 5311-5325,
550 10.5194/acp-14-5311-2014, 2014.

551 Moxim, W. J., Levy, H., II, and Kasibhatla, P. S.: Simulated global tropospheric PAN: Its transport and impact on NO_x, *J. Geophys. Res.*,
552 101, 12621-12638, 10.1029/96jd00338, 1996.

553 Mu, Y., Pang, X., Quan, J., and Zhang, X.: Atmospheric carbonyl compounds in Chinese background area: A remote mountain of the
554 Qinghai-Tibetan Plateau, 112, <https://doi.org/10.1029/2006JD008211>, 2007.

555 Qiu, Y., Ma, Z., Li, K., Huang, M., Sheng, J., Tian, P., Zhu, J., Pu, W., Tang, Y., Han, T., Zhou, H., and Liao, H.: Measurement report:
556 Fast photochemical production of peroxyacetyl nitrate (PAN) over the rural North China Plain during haze events in autumn, *Atmos.*
557 *Chem. Phys.*, 21, 17995-18010, 10.5194/acp-21-17995-2021, 2021.

558 Singh, H. B., and Hanst, P. L.: Peroxyacetyl nitrate (PAN) in the unpolluted atmosphere: An important reservoir for nitrogen oxides,
559 *Geophysical Research Letters*, 8, 941-944, 10.1029/GL008i008p00941, 1981.

560 Škerlak, B., Sprenger, M., and Wernli, H.: A global climatology of stratosphere–troposphere exchange using the ERA-Interim data set
561 from 1979 to 2011, *Atmospheric Chemistry and Physics*, 14, 913-937, 10.5194/acp-14-913-2014, 2014.

562 Sprenger, M., and Wernli, H.: A northern hemispheric climatology of cross-tropopause exchange for the ERA15 time period (1979–1993),
563 *Journal of Geophysical Research: Atmospheres*, 108, 8521, 10.1029/2002JD002636, 2003.

564 Sprenger, M., Wernli, H., and Bourqui, M.: Stratosphere–Troposphere Exchange and Its Relation to Potential Vorticity Streamers and
565 Cutoffs near the Extratropical Tropopause, *Journal of the Atmospheric Sciences*, 64, 1587-1602, 10.1175/jas3911.1, 2007.

566 Stohl, A., Bonasoni, P., Cristofanelli, P., Collins, W., Feichter, J., Frank, A., Forster, C., Gerasopoulos, E., Gäggeler, H., James, P.,
567 Kentarchos, T., Kromp-Kolb, H., Krüger, B., Land, C., Meloan, J., Papayannis, A., Priller, A., Seibert, P., Sprenger, M., Roelofs, G. J.,
568 Scheel, H. E., Schnabel, C., Siegmund, P., Tobler, L., Trickl, T., Wernli, H., Wirth, V., Zanis, P., and Zerefos, C.: Stratosphere-
569 troposphere exchange: A review, and what we have learned from STACCATO, *Journal of Geophysical Research: Atmospheres*, 108, 8516,
570 10.1029/2002JD002490, 2003.

571 Tang, Q., Prather, M. J., and Hsu, J.: Stratosphere-troposphere exchange ozone flux related to deep convection, *Geophysical Research*
572 *Letters*, 38, L03806, 10.1029/2010gl046039, 2011.

573 Taylor, O.: Importance of peroxyacetyl nitrate (PAN) as a phytotoxic air pollutant, *Journal of the Air Pollution Control Association*, 19,
574 347-351, 1969.

575 Wang, T., Wong, H. L. A., Tang, J., Ding, A., Wu, W. S., and Zhang, X. C.: On the origin of surface ozone and reactive nitrogen observed
576 at a remote mountain site in the northeastern Qinghai-Tibetan Plateau, western China, *Journal of Geophysical Research: Atmospheres*, 111,
577 D08303, 10.1029/2005JD006527, 2006.

578 Wei, W., Zang, J., Wang, X., and Cheng, S.: Peroxyacetyl nitrate (PAN) in the border of Beijing, Tianjin and Hebei of China:
579 Concentration, source apportionment and photochemical pollution assessment, *Atmospheric Research*, 246, 105106,
580 <https://doi.org/10.1016/j.atmosres.2020.105106>, 2020.

581 Wolfe, G. M., Marvin, M. R., Roberts, S. J., Travis, K. R., and Liao, J.: The Framework for 0-D Atmospheric Modeling (F0AM) v3.1,
582 *Geosci. Model Dev.*, 9, 3309-3319, 10.5194/gmd-9-3309-2016, 2016.

583 Wu, F., Yu, Y., Sun, J., Zhang, J., Wang, J., Tang, G., and Wang, Y.: Characteristics, source apportionment and reactivity of ambient
584 volatile organic compounds at Dinghu Mountain in Guangdong Province, China, *Science of The Total Environment*, 548-549, 347-359,
585 <https://doi.org/10.1016/j.scitotenv.2015.11.069>, 2016.

586 Xu, W., Lin, W., Xu, X., Tang, J., Huang, J., Wu, H., and Zhang, X.: Long-term trends of surface ozone and its influencing factors at the
587 Mt Waliguan GAW station, China – Part 1: Overall trends and characteristics, *Atmospheric Chemistry and Physics*, 16, 6191-6205,
588 10.5194/acp-16-6191-2016, 2016.

589 Xu, W., Xu, X., Lin, M., Lin, W., Tarasick, D., Tang, J., Ma, J., and Zheng, X.: Long-term trends of surface ozone and its influencing
590 factors at the Mt Waliguan GAW station, China – Part 2: The roles of anthropogenic emissions and climate variability, *Atmos. Chem.*
591 *Phys.*, 18, 773-798, 10.5194/acp-18-773-2018, 2018a.

592 Xu, W., Zhang, G., Wang, Y., Tong, S., Zhang, W., Ma, Z., Lin, W., Kuang, Y., Yin, L., and Xu, X.: Aerosol Promotes Peroxyacetyl
593 Nitrate Formation During Winter in the North China Plain, *Environmental Science & Technology*, 55, 3568-3581,
594 10.1021/acs.est.0c08157, 2021.

595 Xu, X., Zhang, H., Lin, W., Wang, Y., Xu, W., and Jia, S.: First simultaneous measurements of peroxyacetyl nitrate (PAN) and ozone at
596 Nam Co in the central Tibetan Plateau: impacts from the PBL evolution and transport processes, *Atmos. Chem. Phys.*, 18, 5199-5217,
597 10.5194/acp-18-5199-2018, 2018b.

598 Xue, L. K., Wang, T., Zhang, J. M., Zhang, X. C., Deliger, Poon, C. N., Ding, A. J., Zhou, X. H., Wu, W. S., Tang, J., Zhang, Q. Z., and
599 Wang, W. X.: Source of surface ozone and reactive nitrogen speciation at Mount Waliguan in western China: New insights from the 2006
600 summer study, *Journal of Geophysical Research*, 116, D07306, 10.1029/2010jd014735, 2011.

601 Xue, L. K., Wang, T., Guo, H., Blake, D. R., Tang, J., Zhang, X. C., Saunders, S. M., and Wang, W. X.: Sources and photochemistry of
602 volatile organic compounds in the remote atmosphere of western China: results from the Mt. Waliguan Observatory, *Atmos. Chem. Phys.*,
603 13, 8551-8567, 10.5194/acp-13-8551-2013, 2013.

604 Yang, K., Wu, H., Qin, J., Lin, C., Tang, W., and Chen, Y.: Recent climate changes over the Tibetan Plateau and their impacts on energy
605 and water cycle: A review, *Global and Planetary Change*, 112, 79-91, <https://doi.org/10.1016/j.gloplacha.2013.12.001>, 2014.

606 Yao, Q., Ma, Z., Lin, W., Liu, J.-l., Wang, X., Cai, Z., and Han, S.: Transport Characteristics of PAN and O₃ in the Lower Atmosphere of
607 the Boundary Layer in Tianjin in Summer, *environmental science*, 40, 67-75, 10.13227/j.hjkx.201805070, 2019.

608 Yin, X., Kang, S., de Foy, B., Cong, Z., Luo, J., Zhang, L., Ma, Y., Zhang, G., Rupakheti, D., and Zhang, Q.: Surface ozone at Nam Co in
609 the inland Tibetan Plateau: variation, synthesis comparison and regional representativeness, *Atmos. Chem. Phys.*, 17, 11293-11311,
610 10.5194/acp-17-11293-2017, 2017.

611 Yukihiko, M., Hiramatsu, T., Bouteau, F., Kadono, T., and Kawano, T.: Peroxyacetyl nitrate-induced oxidative and calcium signaling
612 events leading to cell death in ozone-sensitive tobacco cell-line, *Plant Signaling & Behavior*, 7, 113-120, 10.4161/psb.7.1.18376, 2012.

613 Zeng, Y., and Hopke, P. K.: A study of the sources of acid precipitation in Ontario, Canada, *Atmospheric Environment*, 23, 1499-1509,
614 1989.

615 Zhang, G., Xia, L., Zang, K., Xu, W., Zhang, F., Liang, L., Yao, B., Lin, W., and Mu, Y.: The abundance and inter-relationship of
616 atmospheric peroxyacetyl nitrate (PAN), peroxypropionyl nitrate (PPN), O₃, and NO_y during the wintertime in Beijing, China, *Science of*
617 *The Total Environment*, 718, 137388, <https://doi.org/10.1016/j.scitotenv.2020.137388>, 2020.

618 Zhang, G., Jing, S., Xu, W., Gao, Y., Yan, C., Liang, L., Huang, C., and Wang, H.: Simultaneous observation of atmospheric peroxyacetyl
619 nitrate and ozone in the megacity of Shanghai, China: Regional transport and thermal decomposition, *Environmental Pollution*, 274,
620 116570, <https://doi.org/10.1016/j.envpol.2021.116570>, 2021.

621 Zhang, J. M., Wang, T., Ding, A. J., Zhou, X. H., Xue, L. K., Poon, C. N., Wu, W. S., Gao, J., Zuo, H. C., Chen, J. M., Zhang, X. C., and
622 Fan, S. J.: Continuous measurement of peroxyacetyl nitrate (PAN) in suburban and remote areas of western China, *Atmospheric*
623 *Environment*, 43, 228-237, 10.1016/j.atmosenv.2008.09.070, 2009.

624 Zheng, X., Wan, G., Chen, Z., and Tang, J.: Measurement and meteorological analysis of ⁷Be and ²¹⁰Pb in aerosol at Waliguan
625 Observatory, *Advances in Atmospheric Sciences*, 25, 404-416, 10.1007/s00376-008-0404-y, 2008.

626 Zhou, L., Hopke, P. K., and Liu, W.: Comparison of two trajectory based models for locating particle sources for two rural New York sites,
627 *Atmospheric Environment*, 38, 1955-1963, 10.1016/j.atmosenv.2003.12.034, 2004.

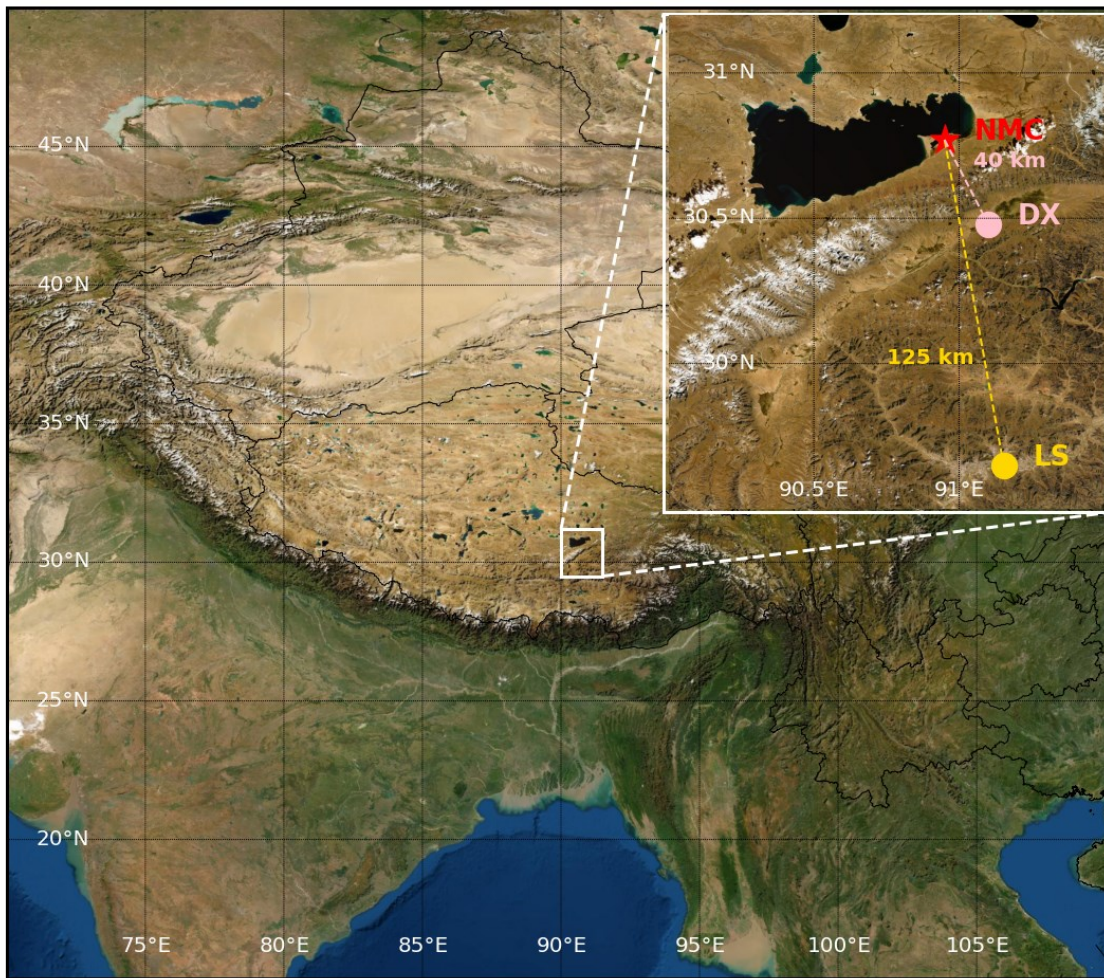
628

629

630 **Table 1** Statistics of trace gases (including O₃, PAN, NO₂, CO, OVOCs, aromatics, alkanes and alkenes), photolysis rates (jO¹D and jNO₂),
 631 meteorological variables, as well as the Y index

Variable	Unit	Spring			Summer		
		all	day (8:00-20:00)	night (20:00-8:00)	all	day	night
O ₃	ppb	59.8±13.4	67.8±9.0	52.2±12.4	53.6±13.2	58.3±12.5	48.8±12.1
PAN	ppb	0.27±0.08	0.30±0.07	0.24±0.07	0.20±0.05	0.21±0.05	0.18±0.05
NO ₂	ppb	0.12±0.05	0.11±0.07	0.13±0.04	0.09±0.05	0.08±0.03	0.10±0.06
CO	ppb	108±26	108±16	107±33	117±29	116±33	118±24
CH ₄	ppm	1.890±0.024	1.884±0.012	1.895±0.030	1.886±0.021	1.883±0.017	1.887±0.024
OVOCs		2.49±2.16	3.10±2.60	1.88±1.34	-	-	-
Aromatics	Propy-Equiv. ppbC	0.56±1.29	0.61±1.74	0.51±0.55	-	-	-
Alkanes		0.47±0.50	0.48±0.59	0.46±0.40	-	-	-
Alkenes		0.59±0.57	0.71±0.68	0.47±0.39	-	-	-
jO ¹ D	10 ⁻⁷ s ⁻¹	-	277±183	-	-	275	-
jNO ₂	10 ⁻⁴ s ⁻¹	-	70±27	-	-	66±29	-
Temperature	°C	4.2±4.1	6.6±3.4	2.0±3.5	9.3±3.5	10.9±3.5	7.7±2.8
RH	%	50±19	41±18	59±17	61±19	55±19	68±17
Cumulated Rain	mm	1.0	0.8	0.2	37.3	24.1	13.2
Wind Speed	m s ⁻¹	4.0±2.6	4.8±2.3	3.3±2.6	3.9±2.3	4.2±2.2	3.6±2.4
Y index	-	1.7±0.9	2.1±0.9	1.4±0.6	0.8±0.3	0.9±0.4	0.7±0.3

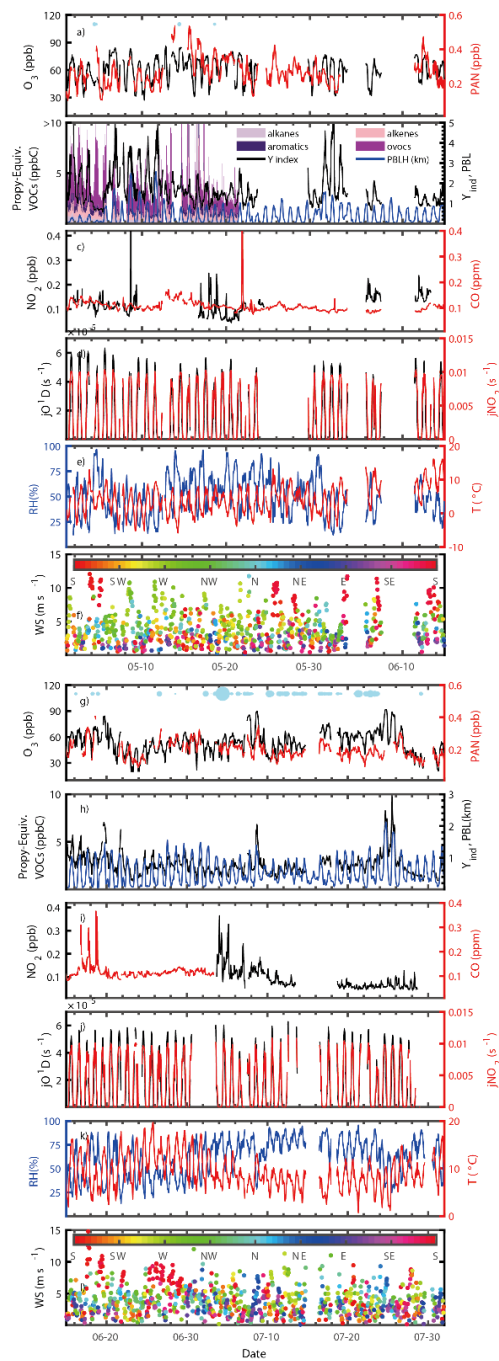
632



633

634 **Figure 1.** Map displaying the locations of the Nam Co site (NMC), Dangxiang (DX) county and Lhasa city (LS). The topographical
635 background figure was provided by the ArcGIS World Imagery Map service ([https://doc.arcgis.com/en/data-appliance/6.4/maps/world-
636 imagery.htm](https://doc.arcgis.com/en/data-appliance/6.4/maps/world-imagery.htm)).

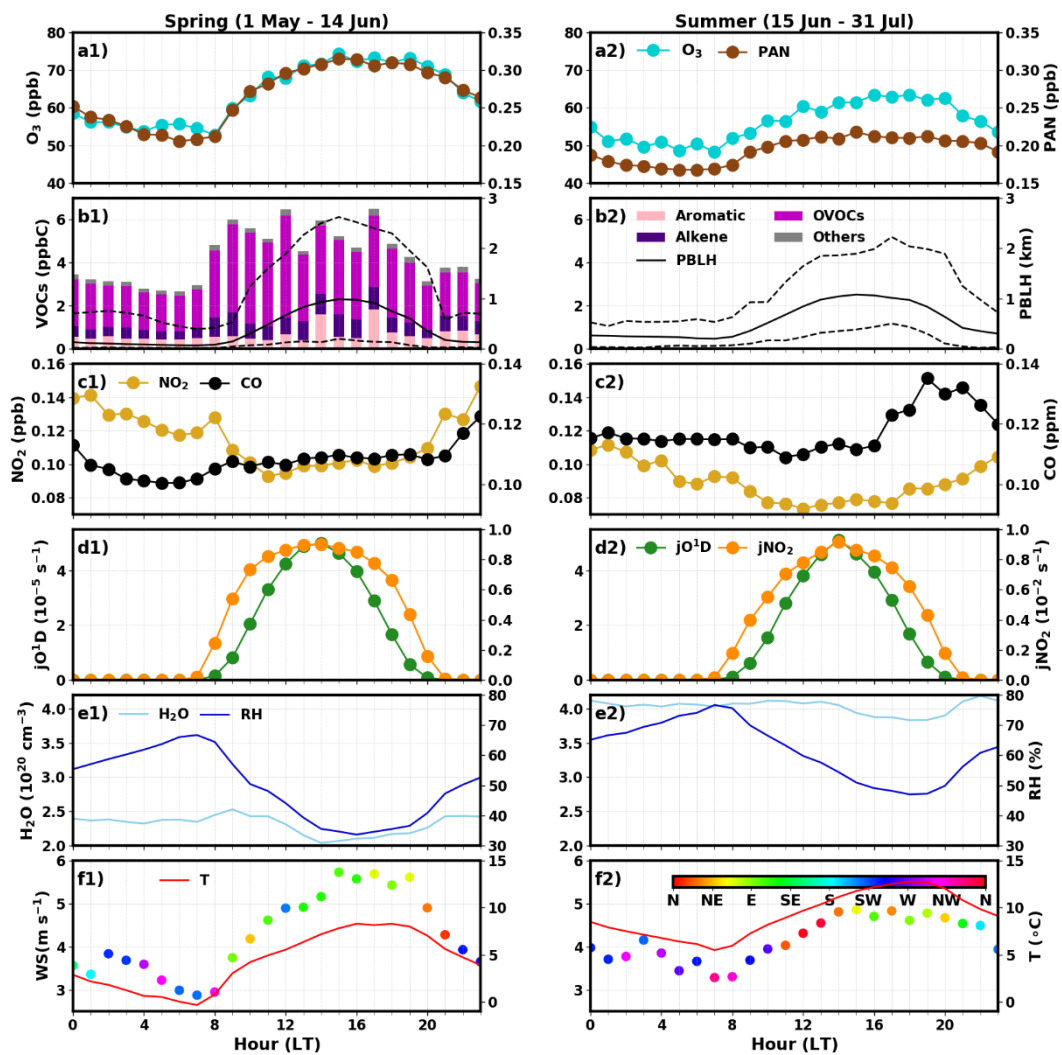
637



638

639 **Figure 2.** Timeseries of (a,g) O₃ (black), PAN (red), (b,h) VOCs (bars), Y index (black), PBLH (blue), (c,i) NO₂ (black), CO (red),
 640 (d,j) jO¹D (black), jNO₂ (red), (e,k) RH (blue), T (red), (f,j) wind speed and wind direction (colored dots) during the spring (a-f, 1
 641 May to 15 Jun.) and summer (g-j, 15 Jul. to 30 Jul.) period at Nam Co.

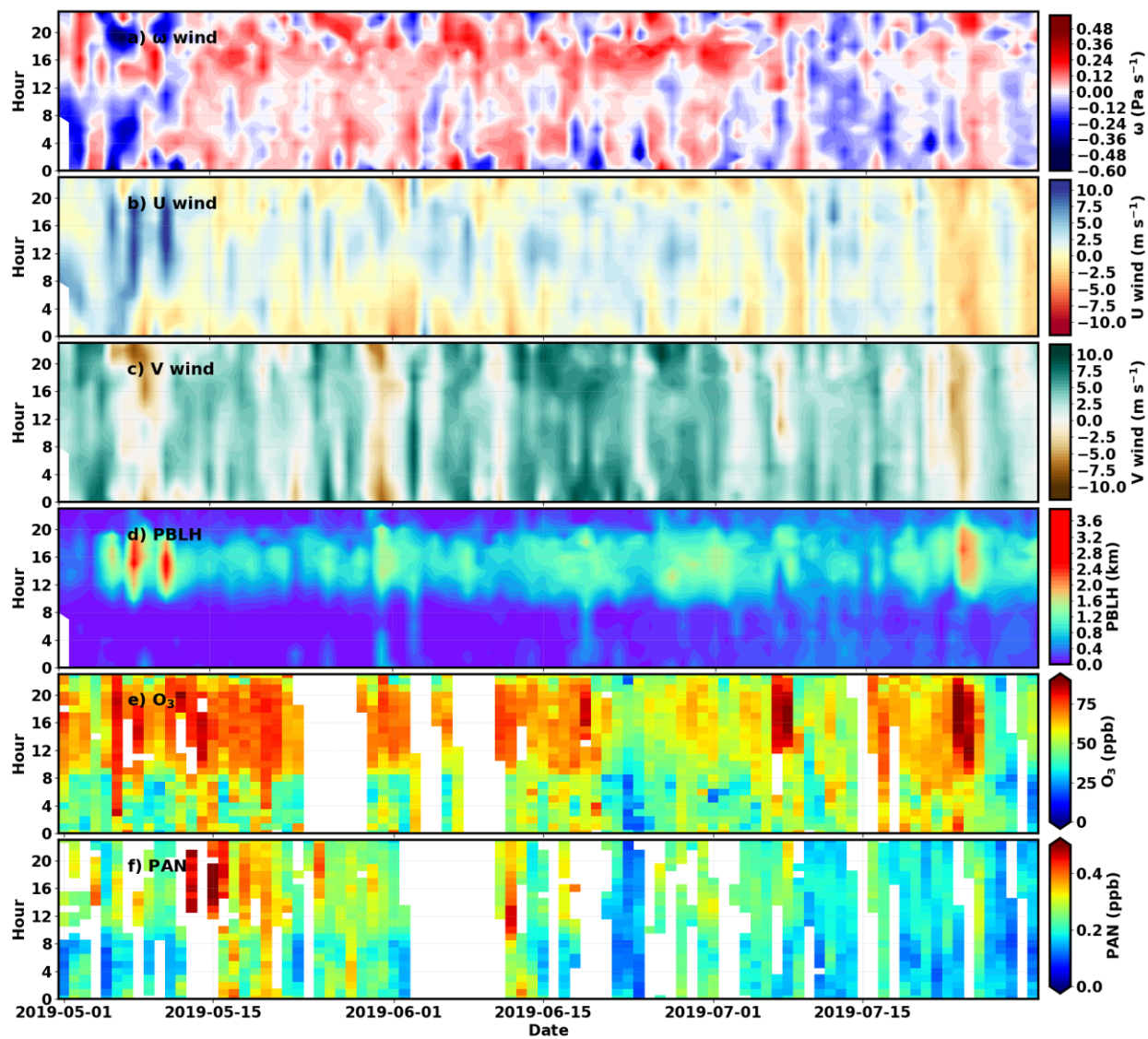
642



643

644 **Figure 3.** Averaged diurnal variations of a) O₃ (blue), PAN (brown), b) VOCs (bars), PBLH (solid line black line: average value, dashed
 645 black lines: minimum and maximum value) c) NO₂ (yellow), CO (black), d) jO¹D (green), jNO₂ (orange), e) H₂O (light blue), RH (dark
 646 blue) and f) temperature (red), wind speed and wind direction, (colored dots) during the 1) spring and 2) summer period, respectively.

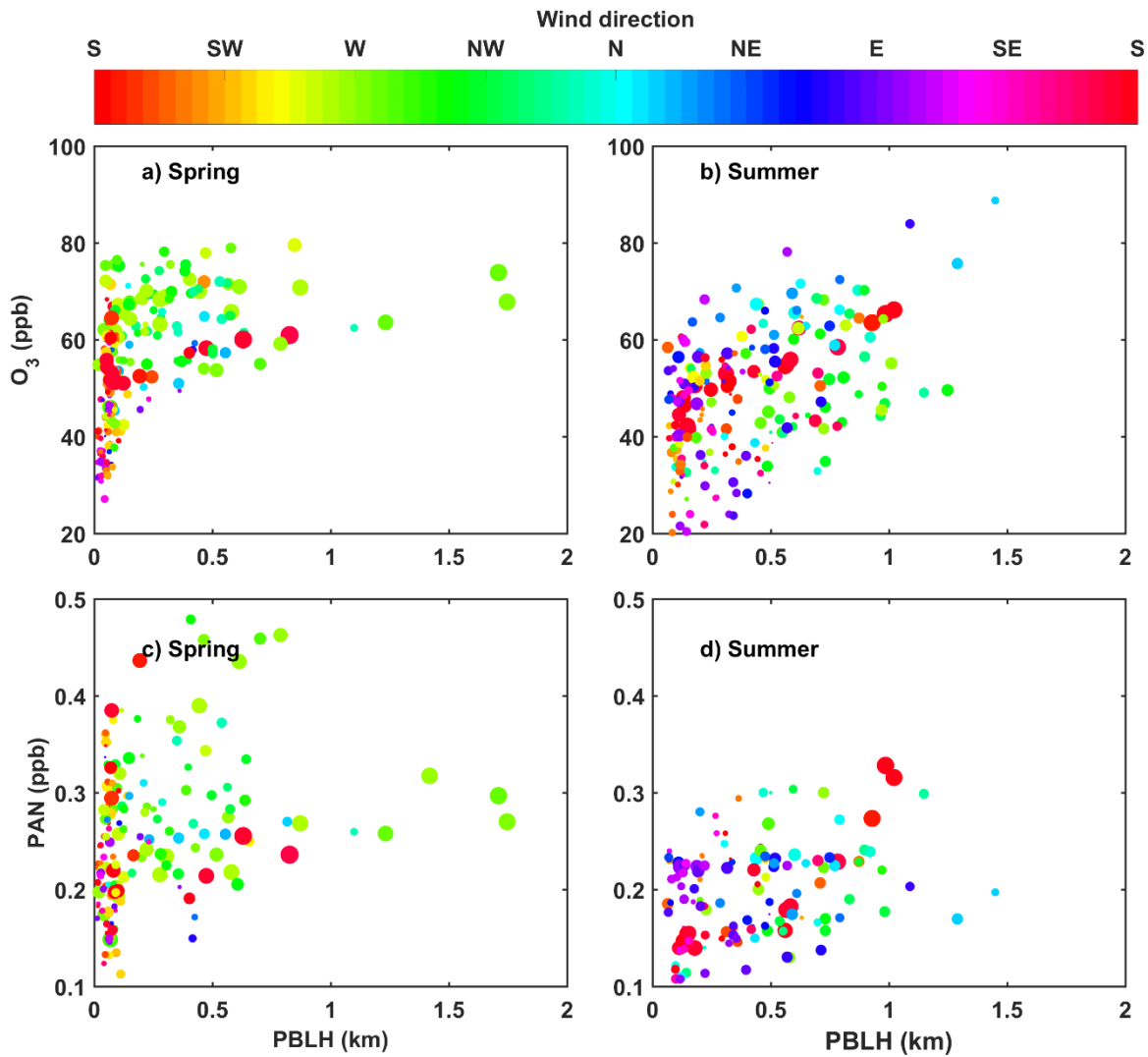
647



648

649 **Figure 4.** Season-diurnal variations of ERA5 550 hPa a) ω wind (vertical wind, Pa s^{-1}), b) u wind (zonal wind), c) v wind (meridional
 650 wind), d) ERA5 PBLH, e) observed surface O_3 and f) PAN between 1 May and 31 Jul 2019 at Nam Co.

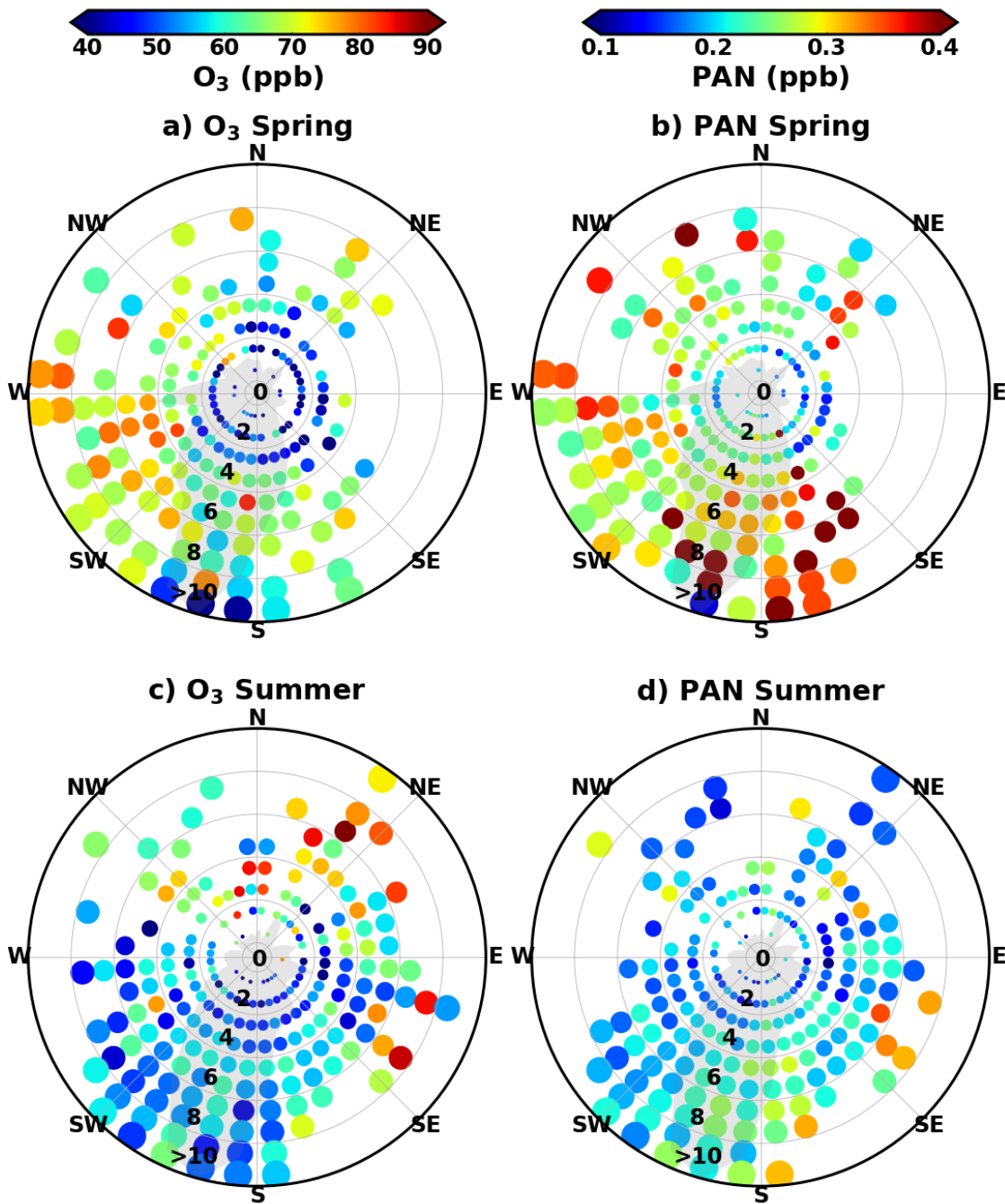
651



652

653 **Figure 5.** Variation of prenoon (6:00-12:00) O₃ (a,b) and PAN (c,d) with PBLH (from ERA5 reanalysis data) during spring (a,c) and
 654 summer (b,d) periods, with wind speeds and directions indicated by sizes and colors of scattered dots (precipitation associated data points
 655 excluded).

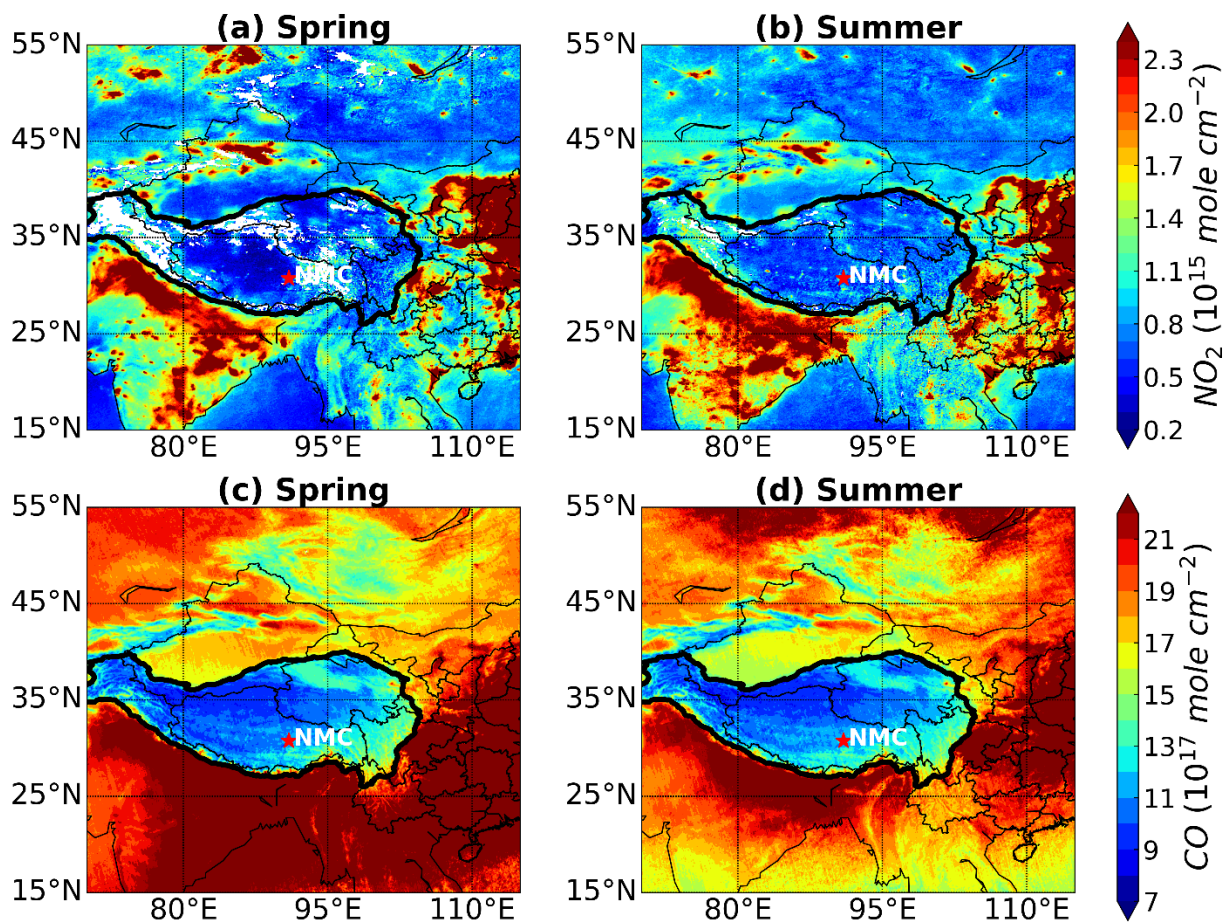
656



657

658 **Figure 6.** Variation of springtime (a,b) and summertime (c,d) O₃ (a,c) and PAN (b,d) concentrations with 2m wind speeds and 500-
659 550 hPa wind directions from ECMWF ERA5 data. Gray shading represents the relative occurrence frequency of wind directions.

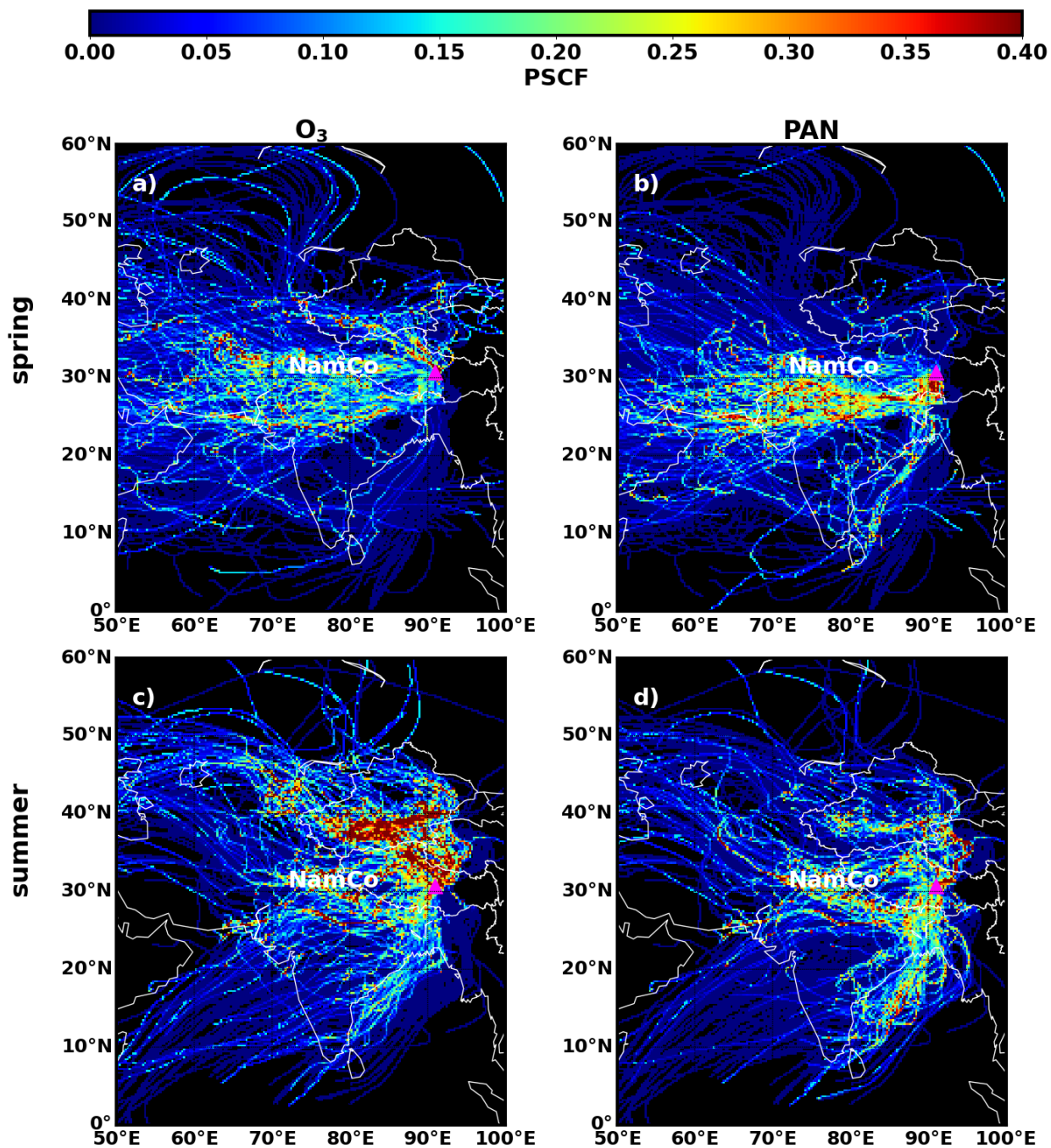
660



661

662 **Figure 7.** TROPOMI NO_2 (a,b) and CO (c,d) column concentration distributions averaged over spring (a,c) and summer (b,d) periods.

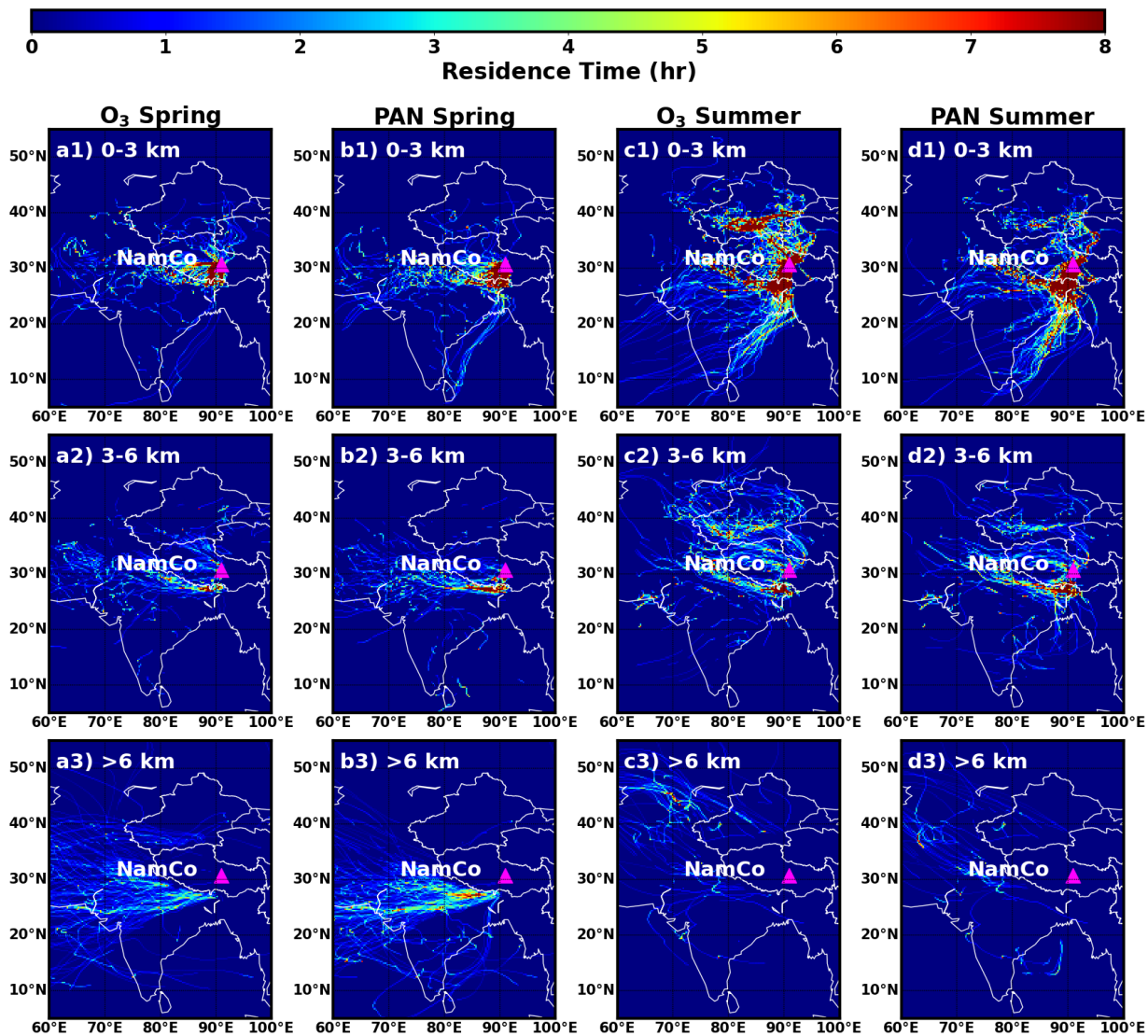
663



664

665 **Figure 8.** Potential Source Contribution Function (PSCF) of O₃ (a,c) and PAN (b,d) during spring (a,b) and summer (c,d) periods.

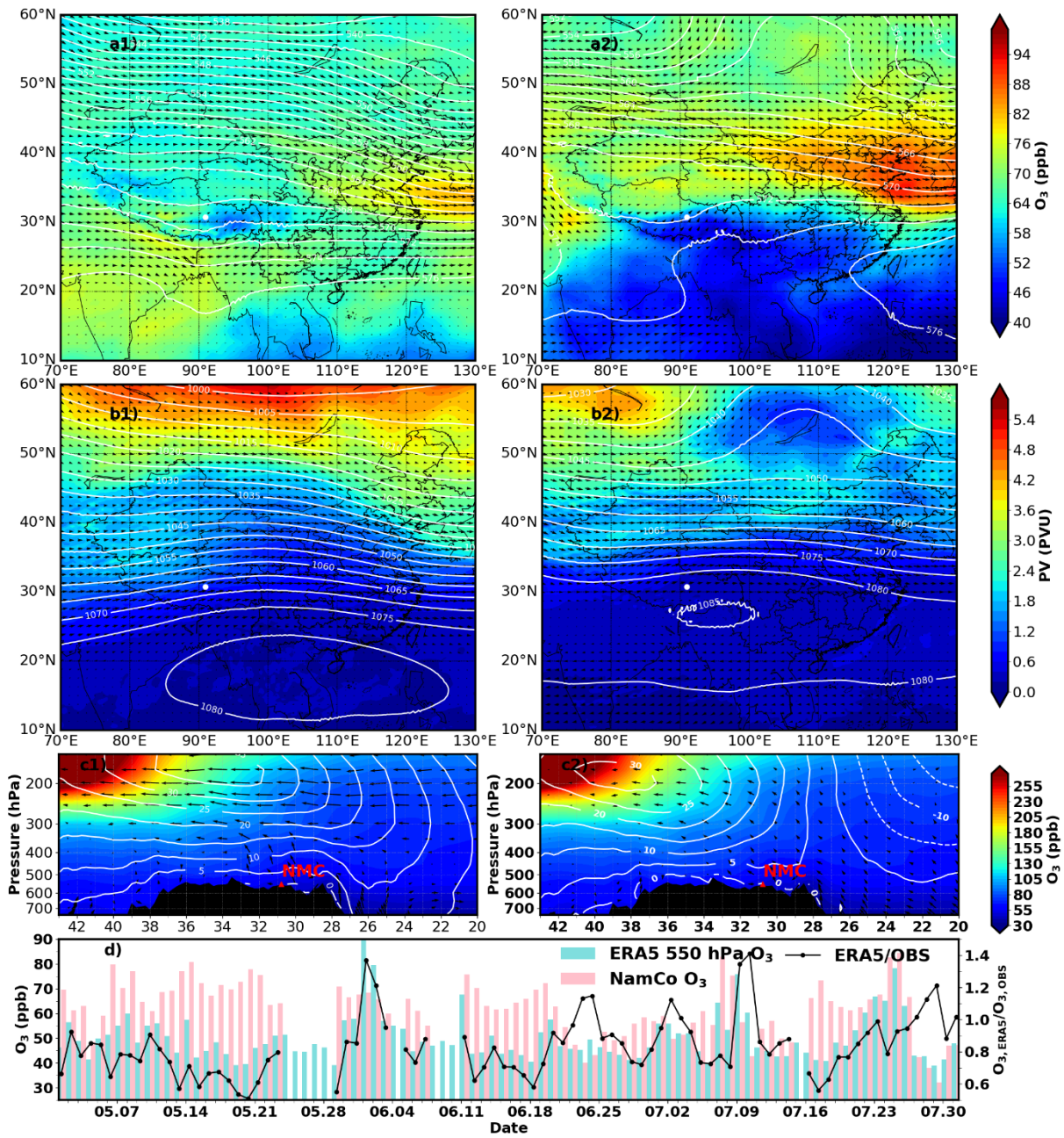
666



667

668 **Figure 9.** Residence time of trajectories associated with O₃ (a,c) and PAN (b,d) above their respective 67th percentiles during spring (a,b)
 669 and summer (c,d) periods within height ranges (above ground level) of 1) 0-3 km, 2) 3-6 km and 3) >6 km.

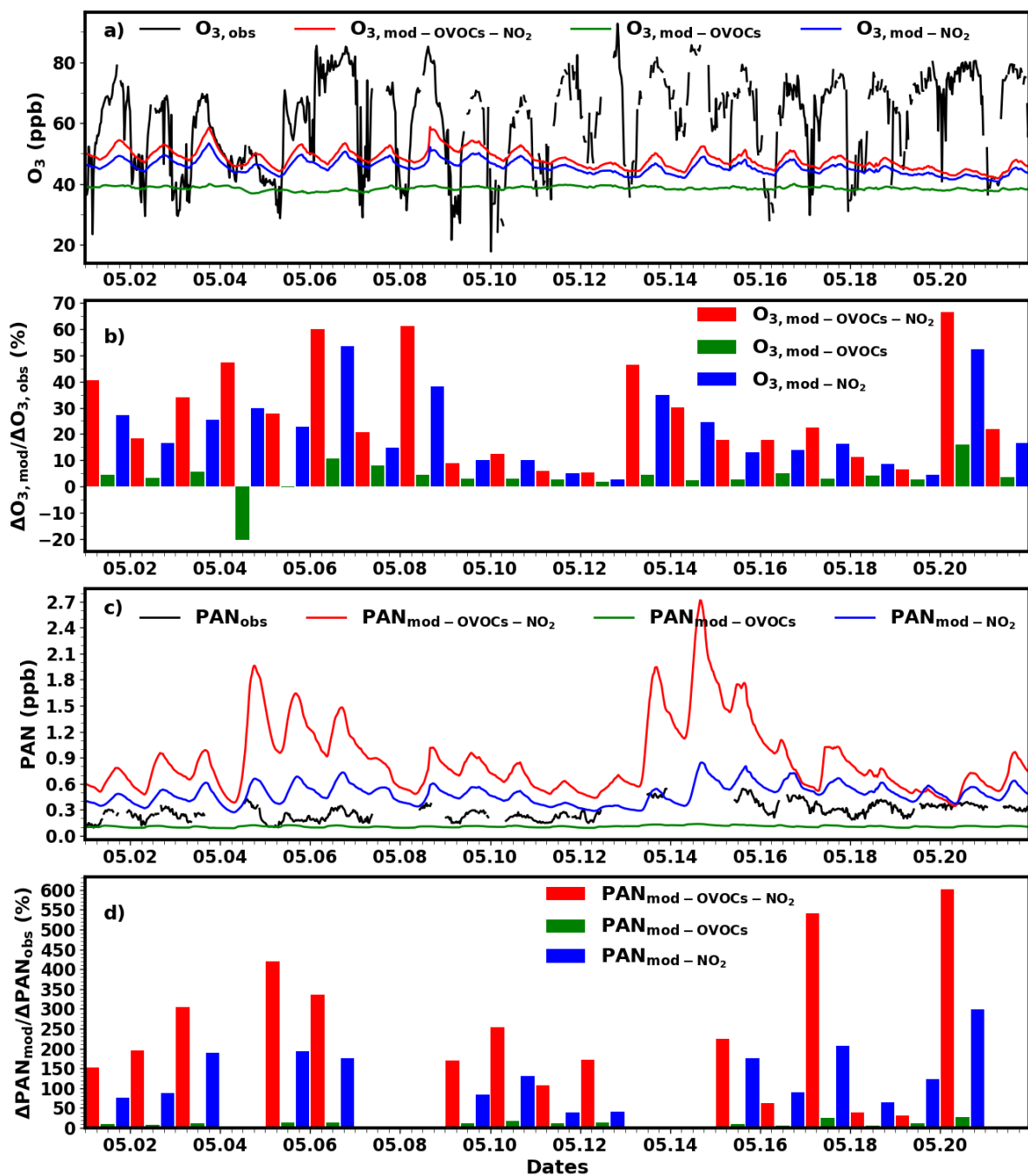
670



671

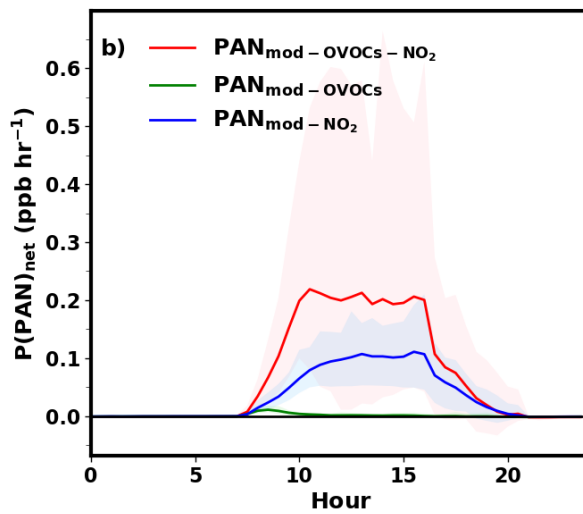
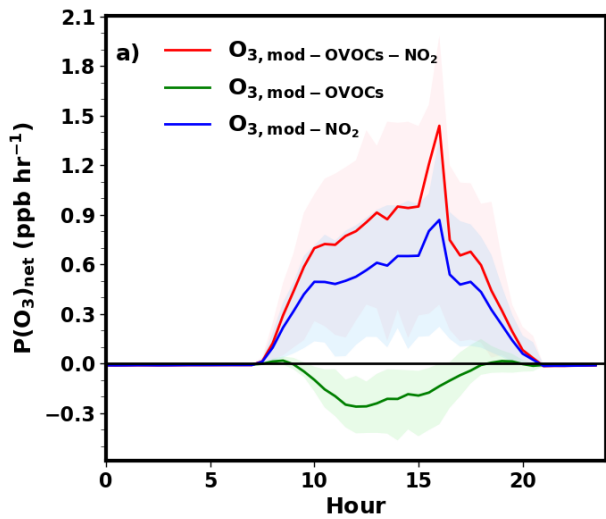
672 **Figure 10.** Distribution of a) ERA5 550 hPa O₃ mixing ratio, geopotential height (white contour lines) and winds (black arrows), b)
 673 250 hPa potential vorticity, geopotential height and winds, c) cross-section of O₃ mixing ratio, u winds (white contour lines), v winds and
 674 vertical velocity (black arrows) at the longitude of Nam Co station and d) the comparison between daytime ERA5 550 hPa (blue bars) and
 675 observed O₃ mixing ratio (pink bars) at Nam Co.

676



677

678 **Figure 11.** a) Observed (black) and modelled O₃ using constraints on OVOCs (green), NO₂ (blue) and both (red), b) percentage of
 679 observed daytime O₃ concentration increment ($\Delta O_{3, \text{obs}}$) that can be explained by those modelled under different constraints ($\Delta O_{3, \text{mod}}$), c)
 680 observed (black) and modelled PAN under OVOCs (green), NO₂ (blue) and both constraints (red), d) percentage of observed daytime PAN
 681 concentration increment ($\Delta \text{PAN}_{\text{obs}}$) that can be explained by those modelled under different constraints ($\Delta \text{PAN}_{\text{mod}}$).



682

683 **Figure 12.** Net production rate of a) O_3 and b) PAN simulated under OVOCs (green), NO_2 (blue) and OVOCs+ NO_2 combined (red)
 684 measurement constraints. Shaded areas represent calculated ranges of 5th to 95th percentiles.